INL/EXT-17-43870

November 2017

INL/US DOE Participation in the Coordinated Research Project FUMAC

Final Report

Giovanni Pastore
Richard L. Williamson
James B. Tompkins
Jason D. Hales

INL/EXT-17-43870

INL/US DOE Participation in the Coordinated Research Project FUMAC

Final Report

Giovanni Pastore
Richard L. Williamson
James B. Tompkins
Jason D. Hales

November 2017

Idaho National Laboratory
Fuel Modeling and Simulation Department
Idaho Falls, ID 83415

Prepared for the
U.S. Department of Energy
Office of Nuclear Energy
Under U.S. Department of Energy-Idaho Operations Office
Contract DE-AC07-99ID13727

Abstract

This report summarizes the contribution of Idaho National laboratory (INL) to the IAEA Coordinated Research Project on Fuel Modeling under Accident Conditions FUMAC. In line with the original research agreement bewtween INL/US DOE/Battelle and IAEA, work at INL has focused on both (i) developments of INL's fuel performance code BISON for the analysis of loss-of-coolant accidents (LOCA) and (ii) simulation of selected FUMAC priority cases. With reference to code development efforts, models were implemented in BISON for high temperature cladding oxidation, Zircaloy solid-solid phase transformation, Zircaloy high temperature creep, cladding burst failure and axial fuel relocation. BISON, analyses were performed of the FUMAC cases (1) MTA-EK tests PUZRY, (2) QUENCH L1 rods 4 and 7, (3) Halden IFA-650.2 and (4) Halden IFA-650.10. In addition, the REBEKA separate effects tests were analyzed, including an effort to investigate 3D cladding response in presence of azimuthal temperature variations. In general, BISON predictions of burst temperature, pressure and time to burst are very reasonable. Predictions of cladding hoop strain are less satisfactory and require additional investigation. Finally, results of 3D simulations indicated that 3D effects are potentially important in fuel rod analysis during LOCAs. BISON results are made available to the FUMAC project as a contribution to the FUMAC benchmark exercise.

Contents

Introduction

To coordinate and support research on nuclear fuel modeling under accident conditions in member countries following the Fukushima accident, the International Atomic Energy Agency (IAEA) sponsored the Coordinated Research Project (CRP) on Fuel Modeling under Accident Conditions (FUMAC).

The US Department of Energy (DOE) has been developing state-of-the-art capabilities to simulate of nuclear fuel behavior within the Nuclear Energy Advanced Modeling and Simulation (NEAMS) and Consortium for Advanced Simulation of Light Water Reactors (CASL) programs. The result is the BISON fuel performance code [1], a modern multidimensional, finite-element based fuel performance code developed at Idaho National Laboratory (INL). Validation work for BISON has focused initially on Light Water Reactor (LWR) fuel during normal operating conditions and power ramps [2]. More recently, significant work has been performed on BISON development and validation for the analysis of accident scenarios such as loss of coolant accidents (LOCA) [3,4] and Reactivity Insertion Accidents (RIA) [5,6].

This report gives an account of INL accomplishments in the framework of the CRP FUMAC. The proposal of INL for participation in FUMAC [7] included

- Developing the BISON fuel performance code to include models for phenomena relevant to fuel rod behavior during LOCAs.
- Simulating some of the FUMAC cases with BISON and providing results to the project.

The work has been performed along the lines outlined in the proposal, with the BISON code having been extended to simulation of LOCA accident scenarios and applied to the analysis of several FUMAC cases. In this report we give an account of this work. In particular, we provide detailed descriptions of BISON developments for LOCA analysis carried out throughout the project and present and discuss BISON simulations. As agreed upon during the First Research Coordination Meeting (RCM1), the FUMAC cases that have been analyzed with BISON are (1) MTA-EK tests PUZRY, (2) QUENCH L1 rods 4 and 7, (3) Halden IFA-650.2, and (4) Halden IFA-650.10. In addition, simulations of the ballooning tests REBEKA were performed and are included in this report, in view of the potential interest to the FUMAC project. This additional work included 3D simulations accounting for azimuthal temperature variations.

The INL contribution does not include an uncertainty analysis on modeling of the Halden test IFA-650.10. This is due to manpower and funding constraints at INL.

The work on BISON development and validation for LOCAs, including the work included in INL's contribution to FUMAC, has benefited from INL's collaboration with the Halden Reactor

Project. This collaboration has recently been strengthened by having BISON developers working onsite in Norway during 2015-2017.

The structure of this report is as follows. In Chapter 1, we summarize BISON enhancements to enable analysis of LOCA behavior. In Chapter 2 we present BISON simulations of the FUMAC cases, as well as additional calculations of potential interest to the project. For each of the considered cases, we include a description of the experiment, details of the BISON setup for the simulations, and a detailed report and discussion of the results. Results are made available to FUMAC for the benchmark exercise. A final chapter provides conclusions and recommendations from the INL activities within FUMAC.

1 BISON developments for LOCA analysis

From the beginning, BISON has incorporated a large-strain mechanics formulation, essential to correctly analyze cladding ballooning during LOCAs. In order to capture the complex material response during accident situations, however, it is also necessary to incorporate in the code specific models dealing with the high-temperature, transient phenomena involved. For this purpose, dedicated material models have been incorporated in the thermo-mechanics analysis framework of BISON. Models are overviewed in this chapter.

BISON's capability enhancements for accident analysis performed during this work and applied to the simulations presented in Chapter 2 include models for high-temperature steam oxidation of Zircaloy cladding, crystallographic phase transformation of Zircaloy, high-temperature cladding creep and cladding failure due to burst [3,4].

In addition, BISON's model of fission gas swelling and release in UO_2 was extended to include a specific treatment of the burst release effect during transients. This transient model was originally developed based on power ramp data [8,9] and has not been re-calibrated and validated yet for LOCA transients. However, it has been applied with some success to RIA design basis accident simulations [6], and can potentially be adapted and applied to the improved simulation of FGR during LOCA transients. In view of its potential for the modeling of fission gas behavior during DBAs, this development is deemed relevant to the FUMAC project and has been included in this report. The development of the transient fission gas behavior model was carried out in collaboration with POLIMI (Italy) and JRC-ITU (European Commission, Germany).

Also, two recent BISON developments for LOCA analysis, i.e., cladding oxidation energy deposition and axial fuel relocation, have not yet been applied to the simulations described in Chapter 2. However, these are new BISON capabilities that are in place and relevant to LOCA analysis, thus they are deemed of potential interest to the FUMAC project and included in this report as an additional contribution. These capabilities will be applied in future LOCA simulations with BISON.

1.1 High-temperature cladding oxidation

The process of oxidation of Zircaloy through an exothermic reaction with the coolant affects both thermal and mechanical performance of the cladding. On the one hand, the growth of a zirconium dioxide (ZrO_2) scale on the cladding outer surface adds to the thermal resistance to heat transfer from the fuel to the coolant and leads to thinning of the metallic wall. On the other hand, oxygen uptake affects the mechanical properties and burst failure behavior of the cladding

Table 1.1: Parameters of the correlations for oxide scale (S) and oxygen mass gain (g) at high temperature [10].

Correlation	A_S (m^2s^{-1})	Q_S/R (K)	A_g ($kg{\cdot}m^{-2}$)	Q_g/R (K)
Leistikov	7.82×10^{-6}	20214	52.42	20962
Cathcart-Pawel	2.25×10^{-6}	18062	36.22	20100
Prater-Courtright	2.98×10^{-3}	28420	3.3×10^{3}	26440

(Section 1.4). Concurrent to the oxidation process, a fraction of the hydrogen generated during the oxidation reaction can be absorbed into the metal, enhancing cladding embrittlement and affecting the phase transformation kinetics of the material (Section 1.2). In the high temperature range (e.g., LOCA) the coolant has become steam, and oxidation proceeds much more rapidly than at normal LWR operating temperatures. Under these conditions, the kinetics of oxide scale growth and oxygen mass gain can be described by a parabolic law, with the reaction rate constant defined as a function of the temperature through an Arrhenius relation [10]:

$$\frac{d\xi^2}{dt} = A \exp\left(\frac{-Q}{RT_I}\right) \tag{1.1}$$

where
ξ is either the oxide scale thickness, ξ=S (m), or the oxygen mass, ξ=g ($kg{\cdot}m^{-2}$)
T_I is the metal-oxide interface temperature (K)
A is the oxidation rate constant (m or $kg{\cdot}m^{-2}$)
Q is the activation energy (J/mol)
R is the universal gas constant (J/mol-K)

Following the recommendations in [10], the BISON model includes correlations for oxide scale growth and oxygen mass gain rates in Zircaloy-2/4 appropriate to different temperature ranges. In particular, the following approach is adopted.

- For metal-oxide interface temperatures from 673 K up to 1800 K, the Leistikov [11] correlation is used. The Cathcart-Pawel correlation [12] is also available and can be chosen as an option. The Leistikov correlation has been selected as reference in view of the larger underlying database, the availability of experimentally determined mass gain for all tests, and the better fit for lower temperature relative to the Cathcart-Pawel correlation [10].
- Above 1900 K, the Prater-Courtright correlation [13] is used.
- Between 1800 and 1900 K, a linear interpolation is made. Linear interpolation between two correlations of Arrhenius type is obtained by a third correlation of the same type [10].

The values of the parameters in Eq. 1.1 relative to the different correlations are given in Table 1.1.

1.2 Phase transformation of the cladding material

Under extreme in-service conditions, e.g., during a postulated LOCA, fuel cladding will be subjected to a rapid increase in temperature (up to 1000-1500K), which involves time-dependent phase transformation of Zr alloy from hexagonal (α-phase) to cubic (β-phase) crystal structure. Modeling the kinetics of crystallographic phase transformation is pivotal for the assessment of the mechanical properties essential for fuel rod integrity (deformation and burst) during a postulated LOCA.

The crucial parameter for the transformation kinetics is the evolution of the volume fraction of the new phase as a function of time and temperature. A model is available in BISON for calculation of the volume fraction of the favored phase in Zircaloy-4 as a function of time and temperature during phase transformation in non-isothermal conditions. The model is based on [14–16]. The phase transformation rate is expressed by

$$\frac{dy}{dt} = k\left(T\right)\left[y_s\left(T\right) - y\right] \tag{1.2}$$

where y is the volume fraction of β-phase, t (s) the time, y_s (/) the steady-state or equilibrium value of y, and k (s^{-1}) the rate parameter. The β-phase equilibrium fraction is represented by a sigmoid function of temperature

$$y_s = \frac{1}{2}\left[1 + tanh\left(\frac{T - T_{cent}}{T_{span}}\right)\right] \tag{1.3}$$

where T_{cent} and T_{span} are material specific parameters related to the center and span of the mixed-phase temperature region, respectively. For Zircaloy-4, $T_{cent} = 1159 - 0.096w$ (K) and $T_{span} = 44 + 0.026w$ (K) [14] are used, with w being the hydrogen concentration in the range $0 \leq w \leq 1000$ wppm (weight parts per million hydrogen). The rate parameter is expressed in the form

$$k = k_0 exp\left[-\frac{E}{k_b T\left(t\right)}\right] + k_m \tag{1.4}$$

where k_0 is a kinetic prefactor, E an effective activation energy, k_b the Boltzmann constant, and k_m a constant. For Zircaloy-4, $k_0 = 60457 + 18129\left|Q\right|$ (s^{-1}) and $E/k_b = 16650$ (K) [14,16] are used, where $Q = dT/dt$ (Ks^{-1}) is the heat rate in the range $0.1 \leq \left|Q\right| \leq 100$ Ks^{-1}. The $\alpha \rightarrow \beta$ transformation is purely diffusion controlled, while the $\beta \rightarrow \alpha$ transformation is partly martensitic. This is represented by the constant k_m given in the form [16]

$$\begin{cases} k_m = 0 & \alpha \rightarrow \beta \\ k_m = 0.2 & \beta \rightarrow \alpha \end{cases} \tag{1.5}$$

The starting temperatures for the onset of $\alpha \rightarrow \alpha + \beta$ and $\beta \rightarrow \alpha + \beta$ phase transformations are calculated as (in kelvin) [14]

$$T_{\alpha \rightarrow \alpha+\beta} = \begin{cases} 1083 - 0.152w & \text{for } 0 \leq Q < 0.1 \text{ } Ks^{-1} \\ \left(1113 - 0.156w\right)Q^{0.0118} & \text{for } 0.1 \leq Q \leq 100 \text{ } Ks^{-1} \end{cases} \tag{1.6}$$

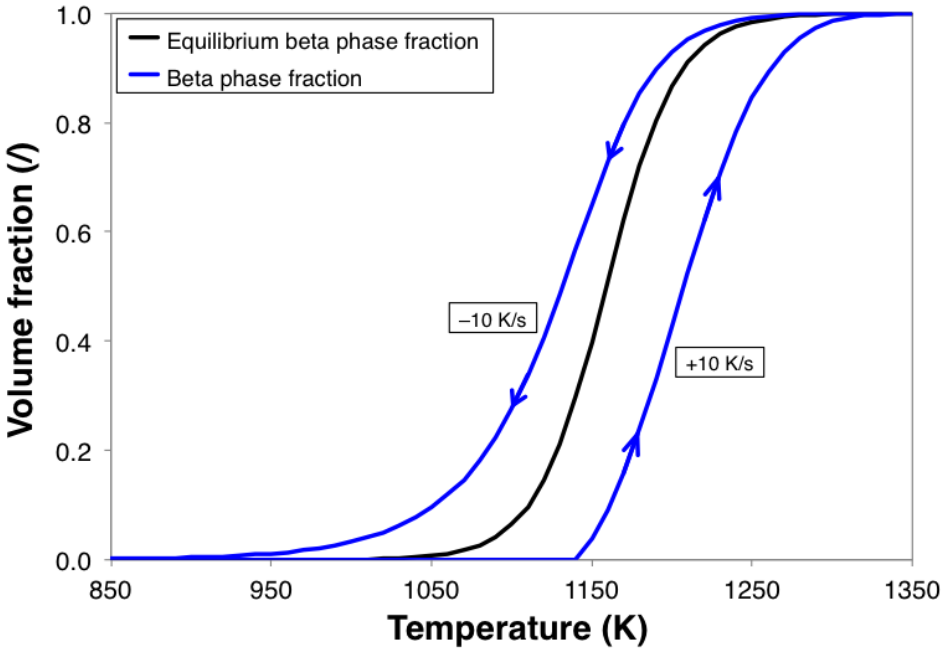

Figure 1.1: Calculated volume fraction of β phase as a function of temperature. Equilibrium conditions (slow temperature variation) and temperature variation rates of ± 10 Ks^{-1} are considered.

$$T_{\beta\to\alpha+\beta} = \begin{cases} 1300 & \text{for } -0.1 < Q \leq 0 \text{ Ks}^{-1} \\ 1302.8 - 8.333\,|Q|^{0.477} & \text{for } -100 \leq Q \leq -0.1 \text{ Ks}^{-1} \end{cases} \tag{1.7}$$

for $0 \leq w \leq 1000$ wppm.

The β-phase volume fraction as a function of time is calculated by numerical integration of Eq. (1.2). As default option, this is accomplished using the second order Adams-Moulton (AM2) method. The backward Euler method is also available. The calculated volume fractions of β phase as a function of temperature at equilibrium and for temperature variation rates of ± 10 Ks^{-1} are shown in Fig. 1.1.

1.3 High-temperature creep of Zircaloy cladding

During a LOCA, outward creep deformation of the cladding tube under the effect of internal pressurization and high temperature drives cladding ballooning and eventual failure due to burst. For LOCA analysis, the large creep deformation of the cladding is defined by a strain rate correlation in the form of a Norton power equation [17–19]:

$$\dot{\varepsilon}_{eff} = A \cdot exp\left(\frac{-Q}{RT}\right) \cdot {\sigma_{eff}}^n, \tag{1.8}$$

Table 1.2: Material parameters used to calculate creep of Zircaloy-4 [19,20].

Phase	$\dot{\varepsilon}_{eff}$ (s^{-1})	A ($MPa^{-n}s^{-1}$)	Q (J/mol)	n (-)
α	any	8737	$321000 \cdot 10^5 + 24.69 \cdot (T - 923.15)$	5.89
50%α–50%β	$\leq 3 \cdot 10^{-3}$	0.24	102366	2.33
	$> 3 \cdot 10^{-3}$	Lin. interp. $\ln(A)$	Lin. interp	Lin. interp.
β	any	7.9	141919	3.78

where $\dot{\varepsilon}_{eff}$ (s^{-1}) is the effective creep strain rate, A ($MPa^{-n}s^{-1}$) the strength coefficient, Q (J/mol) the activation energy for the creep deformation, T (K) the temperature, σ_{eff} (MPa) the effective (Von Mises) stress, and n (-) the stress exponent. The components of the strain tensor are then updated at each time step based on the effective strain increment and a flow rule. The material parameters (Table 1.2) used in the model were obtained from tension tests on Zircaloy-4 tubes [18,19]. In the mixed phase ($\alpha + \beta$) region, interpolations are made to calculate the Norton parameters. Depending on the strain rate, different approaches are adopted [18]:

- For $\dot{\varepsilon}_{eff} \leq 3 \cdot 10^{-3}$ s^{-1}, linear interpolation of ln(A), n, and Q is made between the values for pure α and middle of $\alpha + \beta$ (50%α–50%β) phase, and between 50%α–50%β and pure β phase.

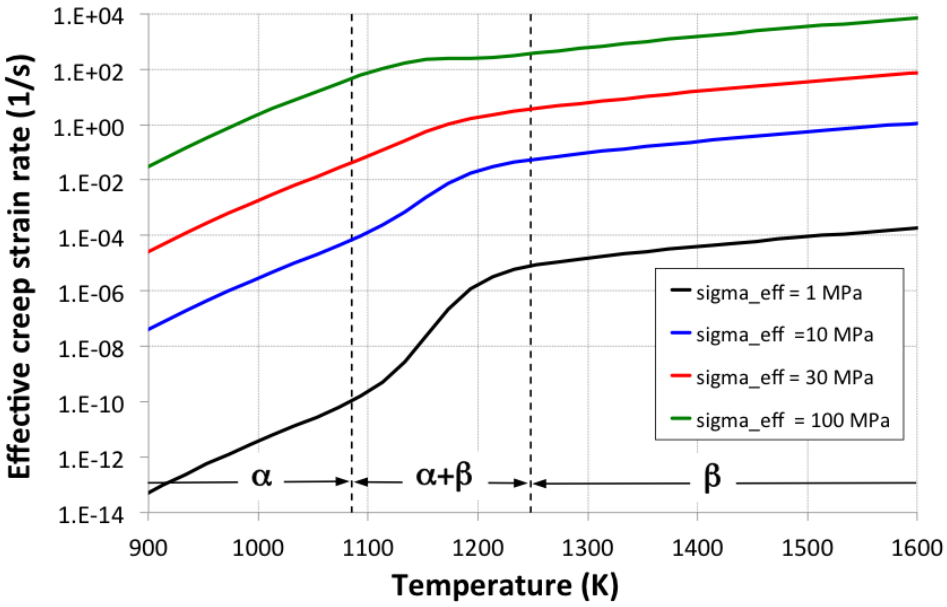

Figure 1.2: Effective creep strain rate of Zircaloy-4 as a function of temperature for different values of the effective stress. The approximate temperature regions corresponding to the different crystallographic phases of the material are highlighted.

- For $\dot{\varepsilon}_{eff} > 3 \cdot 10^{-3}$ s $^{-1}$, it is assumed that the values of ln(A), n, and Q vary linearly between the values for pure α and pure β phase.

To perform the interpolation, the fraction of each phase calculated from a dedicated model as described in Section 1.2 is used. The effective creep strain rate as a function of temperature for different stress values is illustrated in Fig. 1.2.

1.4 Cladding burst failure model

For determining the conditions for failure due to burst of Zircaloy-4 cladding during LOCA accidents, the following criteria have been implemented in BISON:

1. An overstress criterion, which assumes that the time of burst is reached when the local hoop stress equals a limiting burst stress [19]:

$$\sigma_\theta \geq \sigma_b \tag{1.9}$$

   where σ_θ (MPa) is the hoop stress and σ_b (MPa) is the burst stress.

2. A plastic instability criterion, which considers cladding burst at the attainment of a limiting value for the effective plastic strain rate:

$$\dot{\varepsilon}_{pl,eff} \geq \dot{\varepsilon_b} \tag{1.10}$$

   where $\dot{\varepsilon}_{pl,eff}$ is the effective plastic (creep + plasticity) strain rate and $\dot{\varepsilon_b}$ is the limiting value. Following [21], we choose $\dot{\varepsilon_b} = 100\,\mathrm{h}^{-1} \cong 2.78 \cdot 10^{-2}\,\mathrm{s}^{-1}$.

3. A combination of the above criteria, which establishes that cladding burst occurs when either condition 1.9 or 1.10 is fulfilled.

The calculation of the burst stress follows the work of Erbacher et al. [19]. Based on experimental evidence, the burst stress is considered to depend on the temperature and oxygen concentration in the cladding, and is represented by [19]:

$$\sigma_b = a \cdot exp\left(-bT\right) \cdot exp\left[-\left(\frac{\eta - \eta_0}{9.5 \cdot 10^{-4}}\right)^2\right] \tag{1.11}$$

a (MPa) and b (K^{-1}) are constants determined experimentally, and η (-) is the oxygen weight fraction in the cladding. An oxygen weight fraction at fabrication, $\eta_0 = 1.2 \cdot 10^{-3}$, is considered [19]. The current oxygen weight fraction is computed based on the oxygen mass gain from the oxidation model (Section 1.1) as

$$\eta = \frac{2 r_{cl,o}}{\rho_{Zy} \cdot \left(r_{met,o}^2 - r_{cl,i}^2\right)} \cdot g + \eta_0 \tag{1.12}$$

Table 1.3: Material parameters used to calculate the burst stress of Zircaloy-4 [19].

Phase	a (MPa)	b (K^{-1})
α	830	$1 \cdot 10^{-3}$
50%α–50%β	3000	$3 \cdot 10^{-3}$
β	2300	$3 \cdot 10^{-3}$

where $r_{cl,o}$ (m) is the cladding outer radius, ρ_{Zy} = 6550 kg·m^{-3} the density of the cladding metal, $r_{cl,i}$ (m) the cladding inner radius, g (kg·m^{-2}) the oxygen mass (Section 1.1), and $r_{met,o} = r_{cl,o} - S/R_{PB}$ with S (m) being the oxide layer thickness (Section 1.1) and R_{PB}=1.56 the Pilling-Bedworth ratio for Zr. The values for the parameters a and b are given in Table 1.3. In the mixed phase ($\alpha+\beta$) region, linear interpolations of ln(a) and b are made between the values for pure α and middle of $\alpha+\beta$ (50%α–50%β) phase, and between 50%α–50%β and pure β phase [19]. The volume fractions of each phase are calculated by the phase transformation model described in Section 1.2.

As the overstress criterion may lead to unsafe predictions in low-stress situations [21], either the plastic instability or the combined criterion are used.

1.5 Transient fission gas behavior

Fission gas release (FGR) and gaseous swelling in UO_2 fuel are computed in BISON by a physics-based model from [22,23]. This model has been recently extended to allow for the rapid FGR (burst release) during transients [8,9]. This new capability is applied for LOCA transients. Burst release is interpreted as driven by fuel micro-cracking, which is associated with gas depletion of the cracked grain faces during transients and with a corresponding increase in FGR. Gas depletion of a fraction of the grain faces is modeled as a reduction of the fractional grain-face bubble coverage, F. In particular, F is scaled by a factor, f, corresponding to the fraction of non-cracked (intact) grain faces. The reduction of the fractional coverage effectively leads to a decrease of the amount of gas retained in the fuel – consequently, of fission gas swelling – and to a corresponding increase of FGR.

We simplify the micro-cracking process into a purely temperature-dependent behavior, characterized by a micro-cracking parameter, m. We also observe that the process can only affect intact grain faces, and write

$$\left[\frac{df}{dt}\right]_c = -\frac{dm}{dt} f \tag{1.13}$$

Based on the available experimental evidence, the functional form of m is chosen as a temperature-dependent sigmoid function

$$m(T) = 1 - \left[1 + Q\,exp\left(s\frac{T - T_{infl}}{B}\right)\right]^{-\frac{1}{Q}} \tag{1.14}$$

where T_{infl} (K) is the value for the temperature at the inflection point of the function $m(T)$ (inflection temperature), B (K) and Q (–) are parameters related to the temperature-domain width of the phenomenon and the deviation from symmetric behavior during heating/cooling transients, respectively. The value of s (–) is set to +1 during heating transients and to -1 during cooling transients, so that m increases during both heating and cooling. Models characteristics are based on the available experimental evidence of transient FGR (e.g., [24–27]). The inflection temperature corresponds to what has been observed experimentally as a critical temperature for the onset of burst release and is ~1500 C above 20-30 GWd/tU burnup (e.g., [27]). Rather than adopting a discrete temperature threshold, we interpret the observations with a continuous but peaked temperature-dependent release rate. Burnup dependence of micro- cracking, and micro-crack healing, are also accounted for, although details are not given here for brevity (see [8,9] for a more extensive description of the model).

The micro-cracking parameter, m, and the temperature derivative, dm/dT, are plotted in Fig. 1.3. Eqs. 1.13 and 1.14 combined lead to a FGR contribution that activates only during temperature variations (transients). In particular, the FGR during a temperature transient will result from the time integral of Eq. 1.13 during the transient.

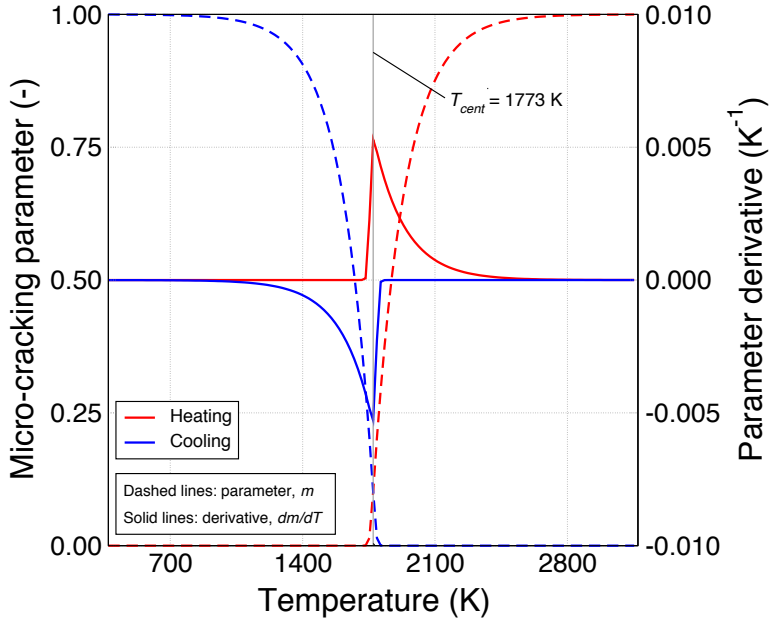

Figure 1.3: Micro-cracking parameter, m, and derivative, dm/dT, as a function of temperature, considering a central temperature equal to 1773 K.

1.6 Cladding oxidation energy deposition

During a LOCA, the coolant flashes to steam which catalyzes the zirconium oxide reaction. At this point the exothermic zirconium oxide reaction is adding a large amount of heat to a fuel system that has limited cooling. This section describes the addition of an Oxide Energy Deposition (OED) model to capture this effect in BISON.

The conversion of zirconium to zirconium oxide is an exothermic reaction and follows the following simple chemical equation [28]:

$$2H_2O + Zr -> 2H_2 + ZrO_2 + Q \tag{1.15}$$

During normal operations the amount of zirconium reacted is small and very gradual, however, during a LOCA the high temperature and stream lead to a substantial amount of the zirconium being reacted, which results in substantial extra energy added to the system. A set of low temperature and high temperature zirconium cladding oxidation models already exist in BISON and is described in Section 1.1. The OED model uses the incremental oxide layer thickness from these models to calculate the energy added to the cladding. In particular, the energy from the zirconium oxide reaction is calculated following equation 4-311 of Vol. 4 of the MATPRO manual [28]. This equation and the inputs can be seen below:

$$P = \left(\frac{0.74}{0.26}\right)\left(\frac{\Delta W}{\Delta t}\right)(2\pi R_0)\,6.45\times10^6[\text{W/m}] \tag{1.16}$$

where:

ΔW is the mass gain per unit surface area due to oxidation at the end of the time step [kg/m^2]
Δt is the timestep [s]
R_0 is the initial cladding outer radius without oxidation [m]
6.45×10^6 is the heat of reaction of zirconium oxide [J/kg]
The ratio $\frac{0.74}{0.26}$ is derived from the assumption that all oxygen forms stoichiometric zirconium oxide. The weight fraction of O_2 in ZrO_2 is 0.26, thus the ratio of zirconium reacted to oxygen added is:

$$\frac{\Delta Zr}{\Delta W} = \frac{1-0.26}{0.26} = \frac{0.74}{0.26} \tag{1.17}$$

where:

ΔZr is the mass of zirconium per unit surface area consumed by oxidation during a given time increment [kg/m^2]
ΔW is the mass gain per unit surface area due to oxidation during a given time increment [kg/m^2]

1.7 Axial fuel relocation

Axial relocation of fuel fragments during a LOCA is a phenomenon that causes redistribution of heat within the rod potentially accelerating cladding failure. As the cladding balloons due to the reduced heat transfer coefficient at its outer surface as a result of the absence of coolant, fragmented and pulverized fuel pellets can fall from upper regions of the rod into the ballooned region. The reduced thermal conductivity of the crumbled fuel and plenum gas mixture, in addition to the increased heat load due to a larger mass of fuel in the ballooned region, results in higher cladding temperatures further exacerbating the cladding distention. The ability to model this complex phenomenon using fuel performance codes is of great importance to ensure accurate predictions of cladding temperature, cladding strain, and the mass of fuel available for dispersal. During FY17 an empirical model was added to BISON to account for the axial relocation phenomenon during LOCAs. The model was originally developed by Jernkvist and Massih [29] and coupled to the FRAPTRAN-1.5 transient fuel performance code. In the following subsections, the key model components are outlined and verification of the numerical algorithm is described.

Fuel Fragmentation and Pulverization

Prior to axially relocating fuel fragments, the amount and size of such fragments need to be quantified. The current model assumes two fuel particle sizes, defined as "fragments" and "pulvers". Fragments are larger fuel particles that exist throughout the irradiation history of the rod and begin forming due to fracture during the first rise to power. Pulvers are the smaller fuel particles that only form at high local burnups due to the disintegration of the high burnup fuel structure at the pellet periphery. For extremely high burnup rods there is potential for the entire pellet to pulverize. The number of radial fragments formed in fresh fuel is defined by [30]:

$$n_f^o = \max\left(1, \min\left(\frac{7q_M^{'} - 8}{17}, 16\right)\right) \tag{1.18}$$

where n_f^o is the number of radial fragments formed in fresh fuel subjected to a power at beginning of life, $q_M^{'}$ is the maximum linear heat generation rate experienced by the fuel in kW/m. Using the initial number of radial fragments calculated above, the number of radial fragments in irradiated fuel is determined by:

$$n_f = \min\left(n_f^o + \frac{\left(16 - n_f^o\right) Bu_{av}}{50}, 16\right) \tag{1.19}$$

where Bu_{av} is the fuel pellet average burnup in MWd/kgHM. Notice that the above equations limit the maximum number of radial fragments to 16. Once the number of radial fragments in irradiated fuel is known, the characteristic side length of the fragments is calculated by:

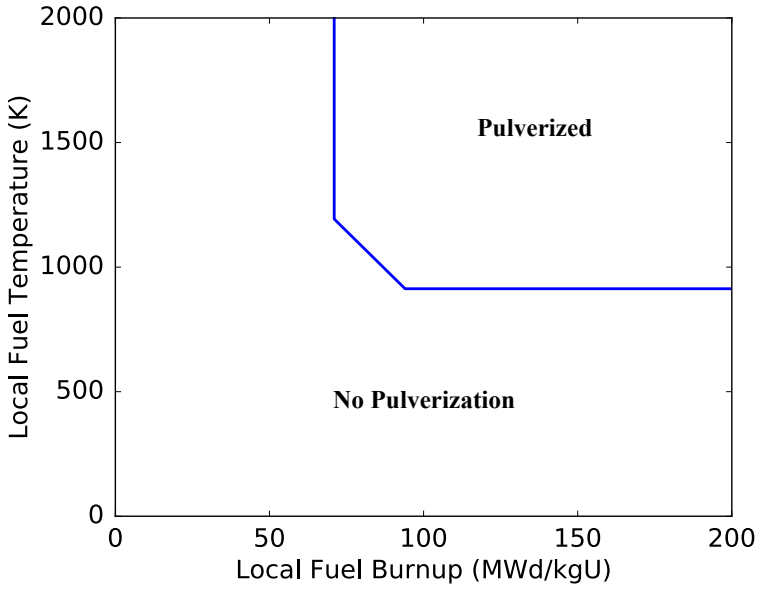

Figure 1.4: Empirical temperature threshold for fuel pulverization [29,31].

$$l_f = D_{FP} \min\left(1, \frac{\pi}{n_f}\right) \tag{1.20}$$

where D_FP is the as-fabricated diameter of the fuel pellet. Before the amount (mass) of fuel that is in fragmented form can be determined, the amount of pulverized fuel must be calculated. The empirical threshold for pulverization is burnup and temperature dependent and illustrated in Figure 1.4 [31]. It is observed that a minimum local burnup of 71 MWd/kgU is required for pulverization. At this burnup the temperature threshold is 1193 K. The threshold decreases linearly with increasing burnup to a value of 913 K at a burnup of 94 MWd/kgU, after which it is constant. It should be noted that despite the temperature threshold being exceeded, pulverization will be prevented if the pellet-to-cladding contact pressure at a particular axial location is greater than 50 MPa [29].

Since the characteristics of pulverized fuel are not well known, Jernkvist and Massih argue that the characteristic side length of the pulvers (l_p) can be treated as a model parameter having a default value of 100 μm. The mass fraction of pulvers (x_p) can be determined from the calculated volume of pulverized fuel to the known total volume of fuel. The mass fraction of fragments is then simply given by $x_f = 1 - x_p$.

Once the mass fractions of both fragments and pulvers are known, an effective packing fraction can be determined using the methodology proposed by Westman [32]. The effective packing fraction (ϕ) is determined by using an internal Newton iteration loop to solve the following:

$$a^2 + 2Gab + b^2 = 1 \tag{1.21}$$

where

$$a = \frac{\phi_p \left(\phi_f - x_f \phi\right)}{\phi \phi_f} \tag{1.22}$$

$$b = \frac{\phi_p \phi_f - \phi \phi_f \left(x_p + x_f \phi_p\right)}{\phi \phi_p \left(1 - \phi_f\right)} \tag{1.23}$$

and G is a parameter that depends upon the difference in shape between the fragments and pulvers. In the preceding equations ϕ_f and ϕ_p represent the packing fraction if the crumbled bed of fuel particles was entirely made up of fragments or pulvers respectively. Jernkvist and Massih suggest values of $\phi_f = 0.69$ and $\phi_p = 0.72$. The G parameter is calculated by:

$$G = \begin{cases} 0.738 \left(D_p^p / D_p^f\right)^{-1.566}, & D_p^p / D_p^f \leq 0.824 \\ 1, & D_p^p / D_p^f > 0.824 \end{cases} \tag{1.24}$$

where D_p^p and D_p^f are the equivalent packing diameters of the pulvers and fragments. The equivalent packing diameter is determined via:

$$D_p = \left(3.9431 - \frac{4.5684}{\psi} + \frac{1.8660}{\psi^2}\right) V_p^{1/3} \tag{1.25}$$

where ψ is the sphericity of the particle and V_p is the volume of the particle. In this model Jernkvist and Massih propose that fragments are prismatic (triangular) in shape and pulvers are octahedral in shape. For a prismatic particle (fragments) whose height is equal to its characteristic side length, $\psi = 0.716$ and $V_p = 0.4330 l_f^3$. For octahedral particles (pulvers), $\psi = 0.846$ and $V_p = 0.4714 l_p^3$.

Once the equivalent packing fraction (ϕ) is known the rest of the model can be calculated as the fuel particle axial relocation loops, the effective thermal conductivity of crumbled fuel, and the effects on heat conduction are all a function of the equivalent packing fraction. In BISON, the pulverization calculation is completed in a material property as it is a function of local burnup whereas the equivalent packing fraction is determined in a userobject as it is a layered averaged quantity.

Fuel Particle Axial Relocation

Since the Jernkvist and Massih axial relocation model was originally developed to be coupled to FRAPTRAN-1.5, a layered approach was taken. FRAPTRAN-1.5 simulates fuel rods as numerous 1D radial slices with generalized plain strain characteristics in the axial direction. Therefore, in the implementation of the axial relocation model in BISON, the recently developed

1.5D capability [33] was used for consistency. Assuming the layers are indexed by k and there are N layers the condition on collapse of the fuel in a given layer is:

$$m_k^M > m_k^i \tag{1.26}$$

where m_k^i is the initial as-fabricated fuel mass in the layer and m_k^M represents the mass in the layer if it is completely filled with crumbled fuel:

$$m_k^M = \phi_k \rho_f \pi L_k R_{cik}^2 \tag{1.27}$$

where ϕ_k is the equivalent packing fraction in the layer, ρ_f is the density of the fuel, L_k is the height of the layer, and R_{cik} is the cladding inner radius for the layer. Two constraints are applied to prevent unrealistic phenomena from occurring. First, relocation can only occur in the downward direction, and second, the amount of fuel that can relocate into a layer is limited by the available mass of fuel existing in all layers above it. These lower (m_k^L) and upper (m_k^U) constraints can be cast into the following equations

$$m_k^L = \sum_{j=1}^{k} m_j^o - \sum_{j=1}^{k-1} m_j \tag{1.28}$$

$$m_k^L = m_k^r + \sum_{j=1}^{k} m_j^o - \sum_{j=1}^{k-1} m_j \tag{1.29}$$

where the superscript m_j^o represents the mass in the j:th layer at the beginning of the timestep (t_o) and m_k^r represents the available mass to be relocated into the k:th layer. Two additional constraints are placed on the movement of mass in Jernkvist and Massih's model: (1) a residual amount of the initial fuel mass will remain in the layer throughout the simulation (denoted by x^r) and (2) the fuel-to-cladding gap must be large enough to accommodate fuel movement (denoted by g^{th}). The algorithm is divided into two loops with the first beginning at the top layer and moving downwards to determine the amount of available mass to be relocated in each layer followed by a loop from the bottom layer to the top that enforces the upper and lower constraints while relocating the mass to the appropriate layers. In the second loop the min and max terms represent a nested conditional statement in the code. The code for the right branch of the loop is shown below for clarity. These two loops are illustrated in Figure 1.5.

```
if (m_k^M < m_k^L)
  m_k = m_k^L
else if (m_k^M > m_k^U)
  m_k = m_k^U
else
  m_k = m_k^M
```

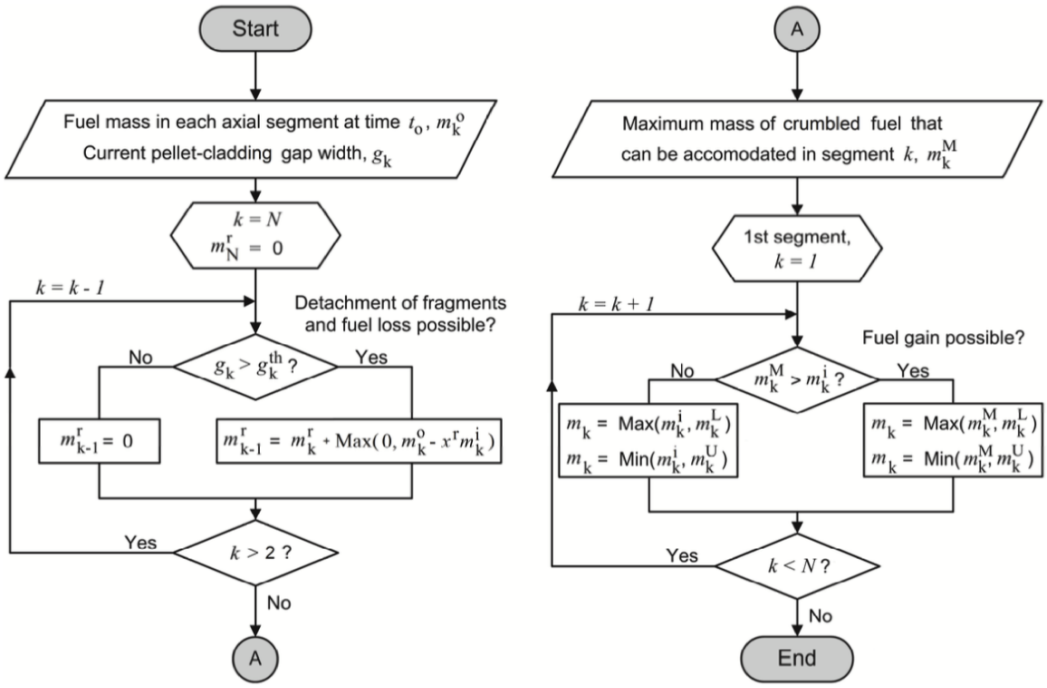

Figure 1.5: The two loops representing the axial relocation algorithm. The left loop is executed first which determines the amount of relocatable mass m^r that can be accommodated in each layer. The second loop enforces the constraints and moves the mass to the appropriate layers. Reproduced from [34].

Thermal Conductivity of Crumbled Fuel

In layers that are crumbled and have accommodated additional fuel the effective thermal conductivity of the fuel and gaseous mixture (i.e., gas from the fuel-to-cladding gap migrates into the voids because the equivalent packing fraction is less than 1) needs to be calculated. The model used by Jernkvist and Massih is that of Chiew and Glandt [35]. The correlation is given by:

$$k_{eff} = \frac{(1-\beta)}{(1+2\beta)(1-\beta\phi)}\left(1+2\beta\phi+\left(K_2-3\beta^2\right)\phi^2\right)k_f \tag{1.30}$$

where β is the reduced thermal polarizability, k_f is the thermal conductivity of the fuel, ϕ is the packing fraction, and K_2 is a function of β and ϕ, defined later. The reduced thermal polarizability is given by:

$$\beta = \frac{k_f - k_g}{k_f + 2k_g} \tag{1.31}$$

where k_g is the thermal conductivity of the gas surrounding the crumbled fuel particles. The K_2 function is approximated by:

$$K_2(\beta,\phi) = K_2^{(0)}(\beta) + K_2^{(1)}(\beta)\,\phi \tag{1.32}$$

where Jernkvist and Massih [29] used best fit approximations to the tabulated values of Chiew and Glandt [35] to obtain:

$$K_2^{(0)}(\beta) = 1.7383\beta^3 + 2.8796\beta^2 - 0.11604\beta \tag{1.33}$$

$$K_2^{(1)}(\beta) = 2.8341\beta^3 - 0.13455\beta^2 - 0.27858\beta \tag{1.34}$$

This effective thermal conductivity is used in the modified version of the heat conduction equation described below for layers that have crumbled (and accommodated additional fuel). In layers that are partially or completely void of fuel, the fuel thermal conductivity is used.

Effects on Heat Conduction

The relocation of fuel throughout the rod during the LOCA transient results in a redistribution of the energy generation. In a 1.5D representation only the radial direction is of great importance in the heat conduction equation. The modified heat conduction in the radial equation is given by:

$$\phi\rho_f c_{pf}\frac{\partial T}{\partial t} - \frac{1}{r'}\frac{\partial}{\partial r'}\left(k_{eff}r'\frac{\partial T}{\partial r'}\right) = \phi q'''' \tag{1.35}$$

where c_{pf} is the specific heat of the fuel. Care must be taken to ensure that in layers where the fuel is crumbled that the outer radius of the fuel is moved outward towards the cladding to take into account the increase in effective diameter of the porous bed of fuel fragments. In the model, Jernkvist and Massih assume that a residual fuel-to-cladding gap (g^r which is a model parameter) remains in the crumbled layers (illustrated in Figure 1.6 adapted from [29]). In layers partially or completely void of fuel the original radial position is used along with the k_f instead of k_{eff}.

Once the fuel has crumbled, the stresses and strains calculated within the fuel do not matter. Therefore, in the BISON implementation, to move the mesh in the crumbled fuel layers a radial relocation eigenstrain is applied that moves the outer surface of the fuel to a position such that g^r remains. This ensures that r' is defined correctly for all layers within the fuel rod.

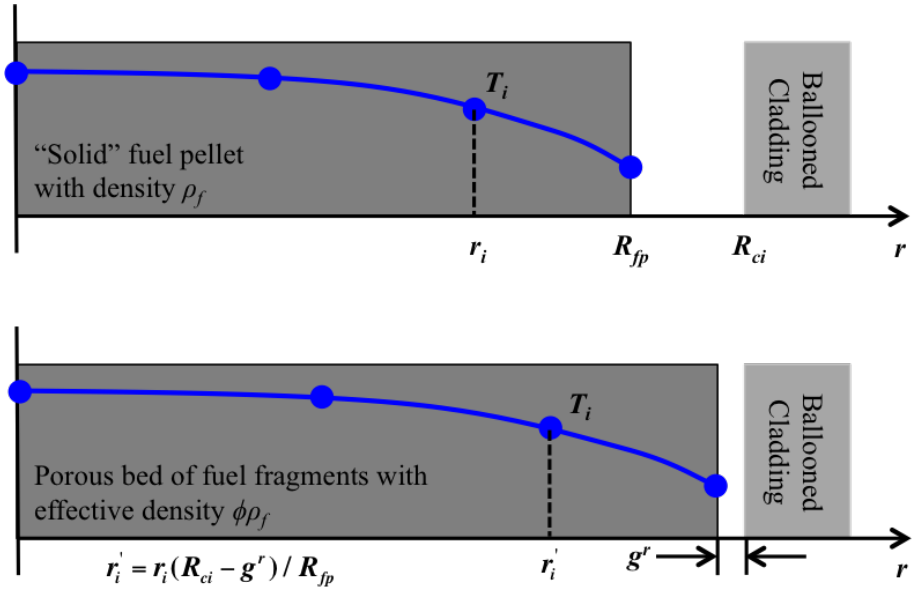

Figure 1.6: Change in fuel geometry and effective fuel density following fuel pellet collapse in the ballooned region of the cladding. A residual gap g^r is assumed to remain.

Verification

To verify the implementation of the axial relocation model governed by the loops shown in Figure 1.5, Jernkvist and Massih [29] propose two test cases denoted as single balloon and twin balloon. In both test cases the active length of the fuel is 3.6 m with a fuel pellet diameter of 9.0 mm. The initial fuel-to-cladding gap is assumed to be zero (i.e., the gap is closed). The effective packing fraction is assumed to be 0.75 after fuel crumbling and 36 equal length axial segments are used. The duration of the simulation is 100 s. The single balloon verification test is to simulate cladding distention that is maximum at the midplane of the active length ($z = 1.8m$). The twin balloon verification test is to simulate the effect of having a spacer-grid at the midplane of the active length.

In the single balloon test the inner cladding radius is varied by:

$$R_{ci}(t,z) = 4.5 \times 10^{-3} + 2.0 \times 10^{-5} t \sin\left(\frac{\pi z}{L_a}\right) \tag{1.36}$$

and in the twin balloon test the inner cladding radius is varied by:

$$R_{ci}(t,z) = 4.5 \times 10^{-3} + 2.0 \times 10^{-5} t \left|\sin\left(\frac{2\pi z}{L_a}\right)\right| \tag{1.37}$$

The BISON results of the these test cases are compared to the digitized results from the Jernkvist and Massih [29] report in Figure 1.7. Three panels are shown for each case representing different times through the duration of the simulation corresponding to 40, 60, and 100 s. The plots show the mass fraction of fuel as a function of axial position. A mass fraction >1 indicates that mass has accumulated in this region and a mass fraction <1 corresponds to a region partially (or completely) void of fuel. As expected in the regions near the maximum cladding ballooning the mass fractions are largest. It should be noted that at the very top of the fuel rod the mass fraction remains as 1. This is because the cladding distention would never be large enough in this top layer to allow fuel to relocate out of it. As is evident in both test cases, the BISON implementation has been verified to be correct as the results match Jernkvist and Massih's results extremely well.

This model will allow first BISON simulations of LOCA experiments that exhibited significant axial fuel relocation, such as the Halden IFA-650.9 test cosidered in FUMAC.

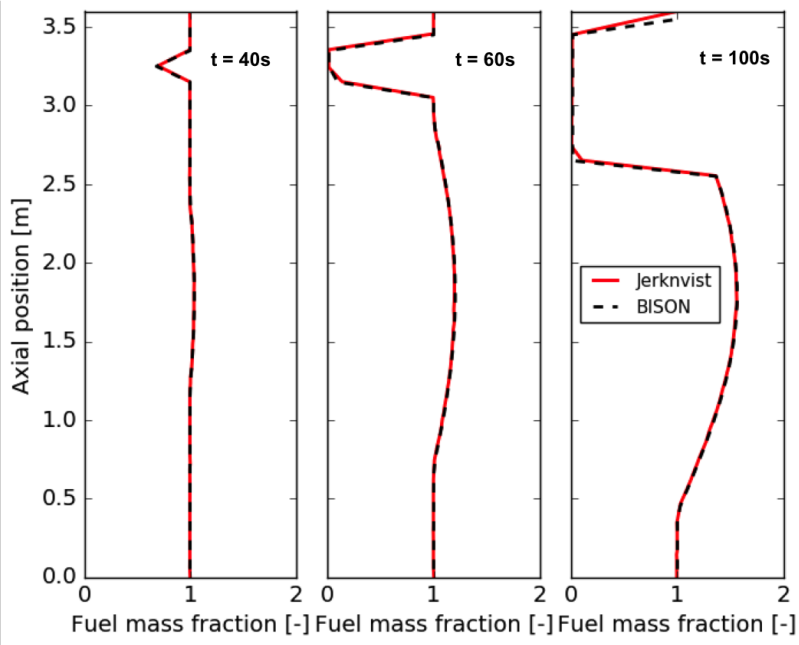

(a)

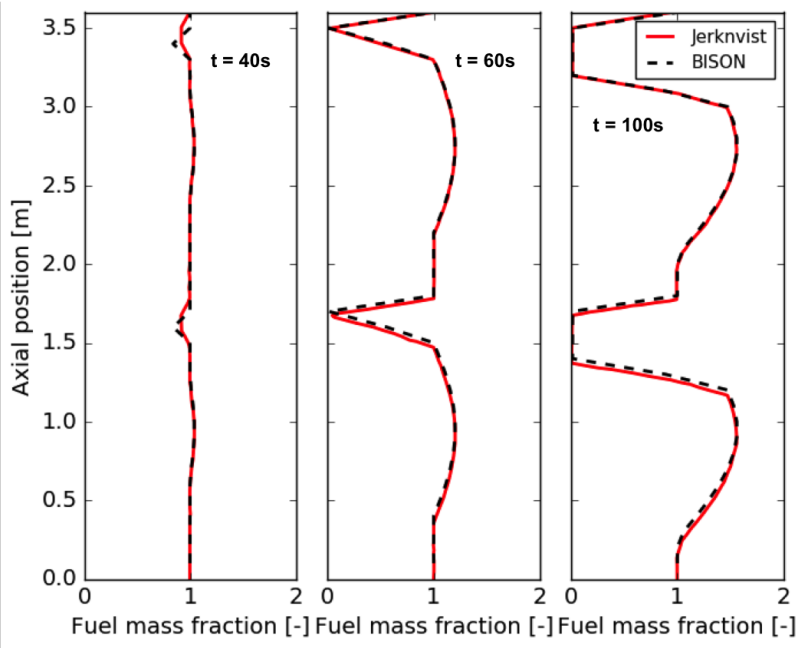

(b)

Figure 1.7: Mass fraction as a function of axial position at 40, 60, and 100 s for (a) single balloon and (b) twin balloon. Jernkvist data obtained from [29].

2 BISON simulations of LOCA experiments

The BISON code, extended with the modeling capabilities described in Chapter 1, was applied to simulations of LOCA experiments, including several FUMAC priority cases. In particular, BISON analyses for the following cases are presented in this chapter:

- MTA-EK separate effects tests PUZRY*
- Separate effects tests REBEKA
- QUENCH L1 rods 4 and 7*
- Halden test IFA-650.2*
- Halden test IFA-650.10*

where the cases labeled with * are FUMAC cases. These are all of the cases agreed upon by INL during the FUMAC RCM1. Although the REBEKA tests were not included in FUMAC, they were analyzed as part of the LOCA validation database for BISON. They are included in this report as part of the INL contribution to FUMAC for completeness and also, for one of the REBEKA cases the 3D capability of BISON was applied to investigate 3D cladding response in presence of azimuthal temperature variations. This produced initial insights into 3D effects during LOCAs, which can be of interest to FUMAC, as discussed during the RCM2 [36]. 3D BISON simulations are presented in Section 2.2.4.

The case EON – Segment 2 was also modeled with BISON [36,37]. However, because this case was later excluded from the FUMAC project, the relative BISON results are not included in this report. More recently, other LOCA cases (not included in FUMAC) were analyzed with BISON. These include the Hardy separate effects experiments [38] and the NRU-MT4 and MT6A fuel rod tests [39,40]. These simulations are also not included in this report. Details can be found in [41].

In the following sections, the analyzed experiments are described and the results of the BISON simulations are presented and discussed.

2.1 MTA-EK separate effects tests PUZRY

INL considered the PUZRY experimental series of isothermal ballooning tests on Zircaloy-4 claddings [42] . All of the 31 PUZRY cases were modeled, although only 6 cases were originally selected for FUMAC. In this Section, we present the overall results for the full set of 31 cases for completeness. We also provide detailed tabulated results for the 6 FUMAC cases.

The PUZRY experimental series [42] was performed in order to study the mechanical behavior (ballooning and burst) of Zircaloy-4 cladding subject to inner pressure transients at high temperature. In particular, the effects of temperature and pressurization rate on the deformation and the failure (burst) pressure were investigated.

2.1.1 Description of the tests

Thirty-one short Zircaloy-4 tube samples were tested in a resistance furnace providing isothermal conditions in the temperature range of 700–1200°C. The inner pressure of the test tube was increased linearly until the burst of the sample. The pressure history was monitored on-line by a computerized data acquisition system. The specimen was placed in a quartz test tube filled with inert gas (Ar). The pressure of the inert gas in the quartz tube was kept at constant 1 bar by means of a buffer volume. After an approximately 1000 s heat-up period the sample was pressurized with Ar gas at a constant pressure increase rate provided by choking with a capillary tube. Different pressurization rates between 0.005–0.263 bar/s could be achieved by using capillary tubes with different diameters. The temperature in the furnace and the cladding inner pressure were recorded by a PC with the data acquisition frequency of 10 records/s.

The specimens were 50 mm long pieces of Zircaloy-4 cladding. The specimens' inner / outer diameters of 9.3 / 10.75 mm corresponded to the parameters of PWR fuel cladding. The samples were closed with Zircaloy end-plugs welded to the cladding in argon atmosphere. The pressurization was performed through a Zircaloy-4 pipe (2.15 mm diameter, 0.25 mm thickness) attached to one end of the specimen. The schematic drawing of the specimen is reported in Figure 2.1. The effect of corrosion on the mechanical performance of Zircaloy-4 cladding was not investigated.

The main characteristics of the PUZRY test series are summarized in Table 2.1.

2.1.2 Setup of BISON simulations

Details of the BISON setup adopted for the calculations are as follows.

- Finite-element 2D axisymmetric models of the cladding tubes were used.
- Taking advantage of the symmetry of the problem, only the lower half of the heated cladding length was modeled.

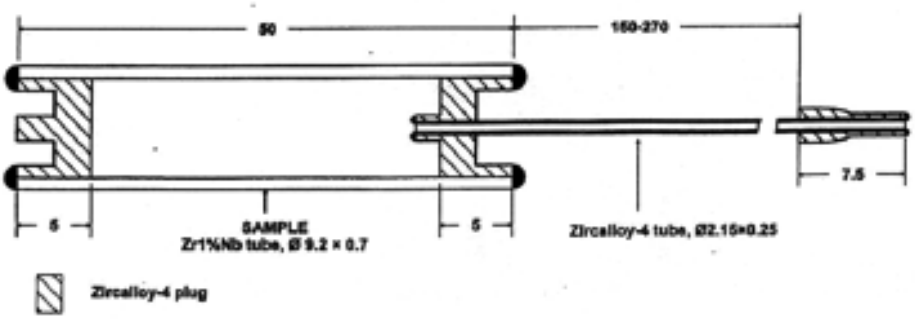

Figure 2.1: Drawing of the tube specimen for single-rod ballooning tests performed at AEKI [42]. Note that Zircaloy-4 tubes were used for the PUZRY tests.

Table 2.1: Main characteristics of the PUZRY test series [42].

Tube specimens	
Alloy	Zircaloy-4
Inner radius (mm)	4.65
Thickness (μm)	725
Length (mm)	50
ZrO_2 layer (μm)	0
End plugs	Zircaloy-4
Experimental conditions	
Temperature range (°C)	700–1200
Heating rate	isothermal tests
Pressure range (bar)	0–106
Pressurization rate (bar/s)	0.005–0.263
Atmosphere	Ar
Instrumentation	Pressure sensor, temperature sensor
Data acquisition (records/s)	10
Number of specimens tested successfully	31

- End plugs were considered by preventing radial motion (i.e., applying zero radial displacement boundary conditions) to the tube inner surfaces in correspondence of the plugs. These correspond to the 5 mm end sections of the cladding (see Fig 2.1).
- Time-dependent pressures were simulated by Dirichlet pressure boundary conditions applied to the tube inner and outer walls.
- The furnace heating was simulated by a Dirichlet temperature boundary condition applied to the tube outer wall. In the PUZRY database [42], tubes temperature profiles along the axial direction are not given. However, applying a perfectly uniform temperature axially would lead to a distributed ballooning along the tube, while several experiments showed localized ballooning with maximum strain and burst occurring near the tube's mid-plane.

This can be interpreted as associated with axial temperature variations that, albeit small, lead to significant strain axial variations by virtue of the strong (exponential) temperature dependence of the creep rate. To account for this, we included a slight axial temperature variation in the BISON simulations. Within FUMAC, Katalin Kulacsy communicated that axial temperature variations of 5-6 K along the central 50 mm section of the furnace can be expected, based on measurments performed in another furnace [43]. On this base, in the BISON simulations we applied a linear temperature profile (simplest possibility in absence of detailed indications) with the maximum temperature applied at the mid-plane (consistent with experimental observations of localized ballooning close to the mid-plane of the specimen). The overall (tube end to tube mid-plane) variation was made equal to 6 K, with the average (tube quarter-length) temperature being equal to the experimental value.

- Prior to the pressure transient, we considered the initial heat-up period by applying atmospheric (0.1 MPa) pressure to both sides of the tube and ramping the temperature up from ambient (300 K) to the test temperature over 1000 s. The inner pressure transient from 0.1 MPa at the experimental rate was applied afterwards, under isothermal conditions. Outer tube pressure was kept constant at 0.1 MPa.
- The combined overstress and plastic instability criterion for cladding burst failure (Section 1.4) was used.

2.1.3 Results

The simulation results for the 31 PUZRY cases are compared to the available experimental data. Figures 2.2 and 2.3 show the comparisons between BISON predictions and experimental data of cladding inner pressure at cladding burst and time to burst, respectively. Note that the axes in these plots have a logarithmic scale. The accuracy of BISON predictions appears to be reasonable.

We also present the BISON results in terms of maximum hoop strain. This area is notoriously difficult for fuel performance codes, even more for LOCA calculations whereby very high strain rates are reached as cladding burst is approached (see, for example, Figure 2.11 in Section 2.2). This implies that the maximum strain reached in the calculation is very sensitive to the specific criterion adopted to determine the time of rod burst (thus, the final time of the calculation and the time at which strain is considered), since small differences in the final time may correspond to large differences in the maximum strain. This has been clearly demonstrated by a previous study by JRC-Karlsruhe where different failure criteria were tested in cladding balloning and bust simulations with the TRANSURANUS code [21]. Comparisons of BISON calculated maximum cladding strains to experimental data for the 31 PUZRY cases are shown (on a linear scale) in Figure 2.4. Predictions deviate from experimental data by up to a factor of 3. Average deviation is of a factor of $\sim$1.7.

Again, a high sensitivity is expected of the calculated strain at burst to the adopted burst criterion and to the relative uncertainties (e.g., creep model, temperature). As mentioned above, for the

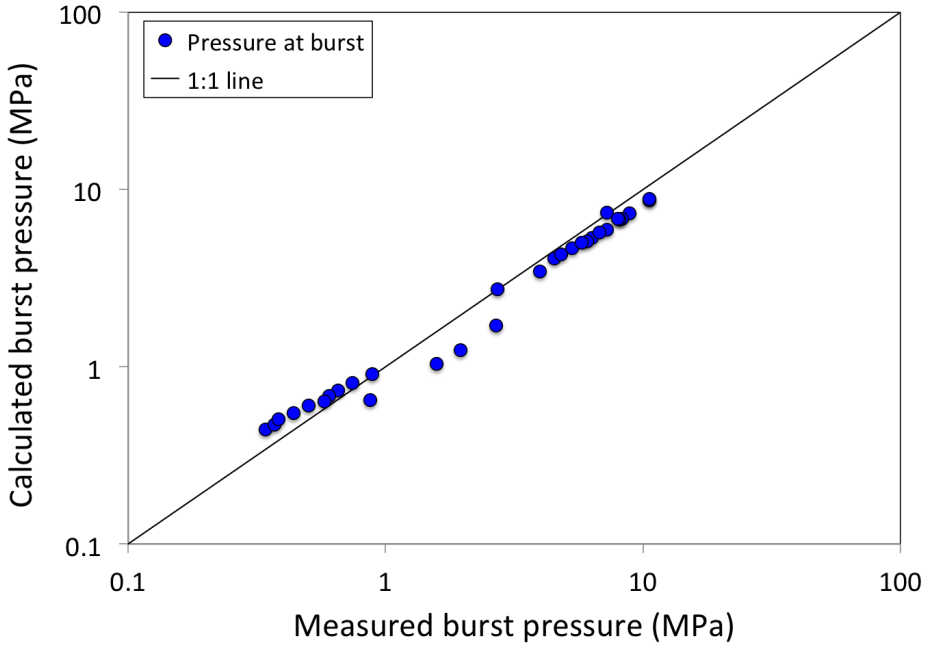

Figure 2.2: Comparison of calculated and measured tube inner pressures at burst for the PUZRY cases.

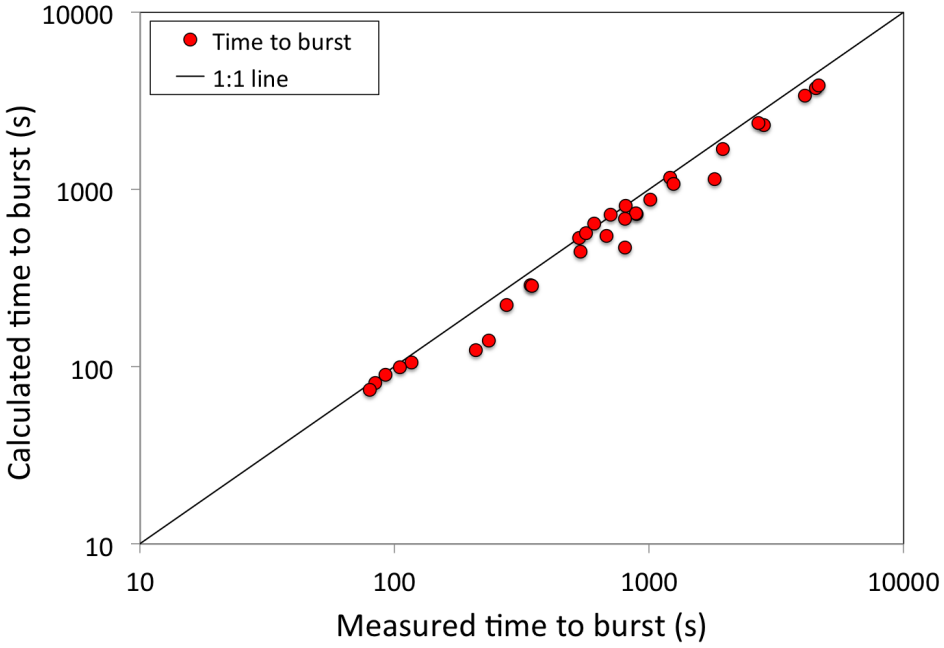

Figure 2.3: Comparison of calculated and measured time to burst for the PUZRY cases.

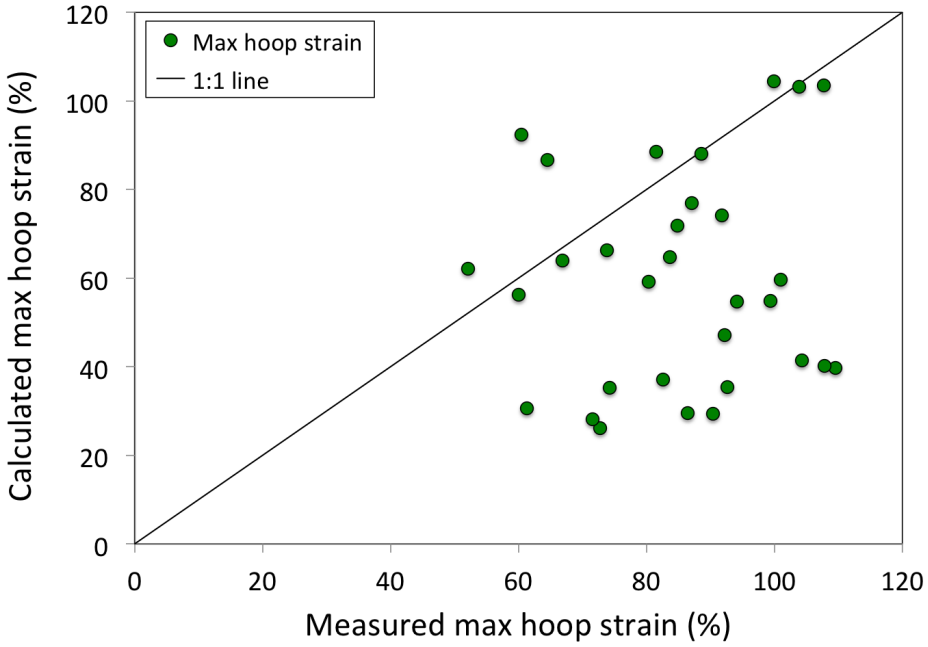

Figure 2.4: Comparison of calculated and measured maximum hoop strain for the PUZRY cases.

PUZRY simulations we adopted a combined overstress and plastic instability burst criterion in BISON (Section 1.4). Further investigation and sensitivity analysis of the dependence of calculated strains upon the choice of the burst criterion (e.g., in line with [21]) is of interest in perspective. Besides this, further developments of the cladding creep model (e.g., considering anisotropic creep) may also improve strain predictions.

Calculated and experimental burst times are also plotted as a function of test temperature in Figure 2.5. The reduction of the burst time as a function of the temperature is reproduced. Deviations of predictions from the experimental data appear to increase at the lower test temperatures.

In Figures 2.6 and 2.7, we present comparisons between BISON predictions and experimental data of burst pressure and time to burst as a function of test temperature, for the 6 FUMAC cases only. Again, accuracy is very good for the higher temperature cases and grow worse at lower temperatures. Higher discrepancies between calculations and experiments at the lower temperatures may indicate that deviations may be partly due to anisotropic creep behavior, which is not considered in the BISON model at this time and characterizes alpha-Zr (i.e., in absence of phase transition to beta-Zr at high temperature, see Section 1.2) [18,19,19].

In view of the FUMAC benchmark exercise, detailed BISON results and experimental data for the 6 PUZRY cases included in FUMAC are tabulated in Table 2.2.

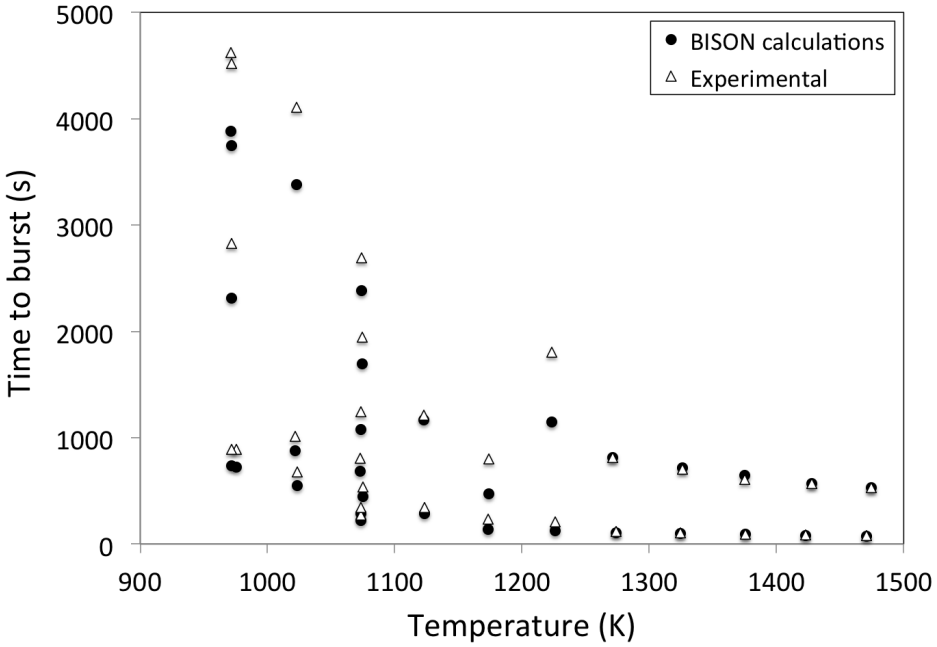

Figure 2.5: Calculated and measured time to burst as a function of test temperature for the PUZRY cases.

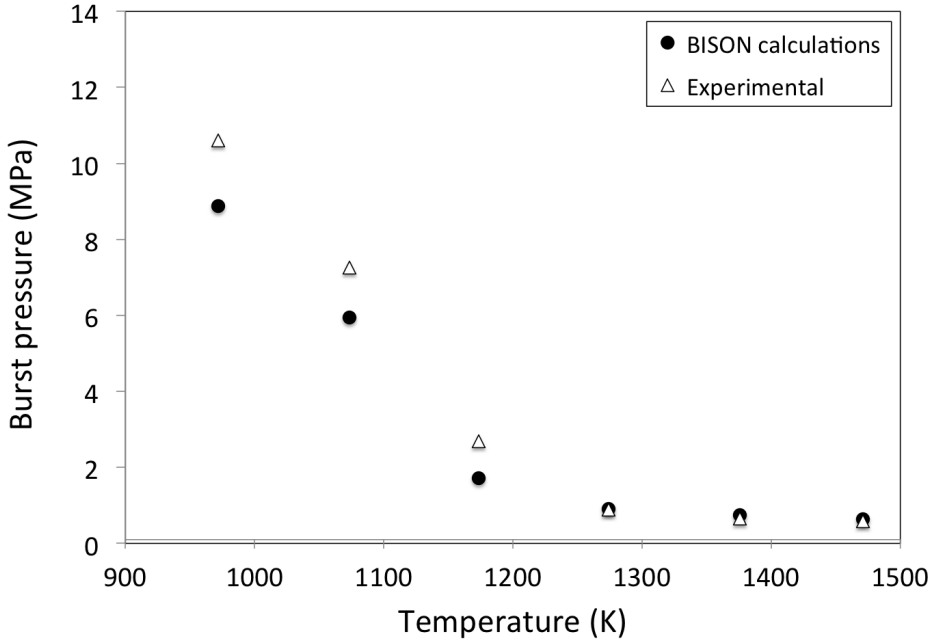

Figure 2.6: Calculated and measured tube inner pressures at burst as a function of test temperature for the 6 PUZRY cases included in FUMAC.

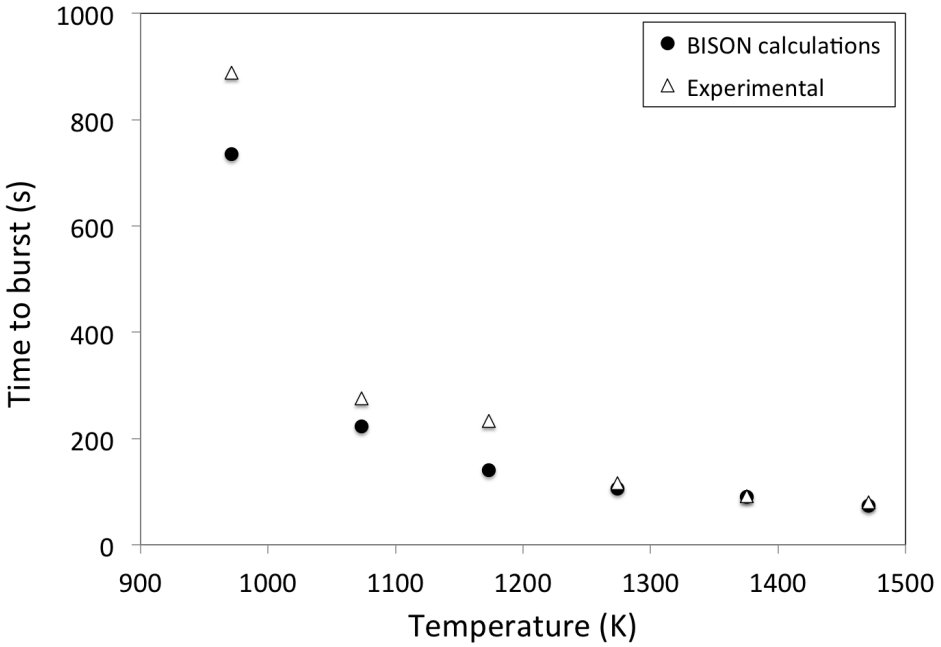

Figure 2.7: Calculated and measured time to burst as a function of test temperature for the 6 PUZRY cases included in FUMAC.

Table 2.2: Experimental data and BISON predictions for the 6 PUZRY experiments selected in the FUMAC project. Time to burst is intended from the beginning of the transient.

Rod	Temperature (K)	Burst pressure (MPa)		Time to burst (s)		Max hoop strain (%)	
		Experiment	BISON	Experiment	BISON	Experiment	BISON
8	1274	0.890	0.906	116.7	105.7	80.37	59.17
10	1376	0.653	0.737	92.0	89.8	72.76	26.13
12	1471	0.578	0.636	80.0	74.1	71.62	28.11
18	1173	2.689	1.717	233.7	140.5	74.29	35.3
26	972	10.605	8.874	888.8	735.4	100.97	59.63
30	1074	7.251	5.951	275.7	222.5	104.28	41.44

2.2 Separate effects cladding tests REBEKA

The REBEKA separate effects tests [19,20,44] are temperature transient tests in steam performed on single PWR-size Zircaloy-4 tubes at a variety of internal pressures and heating rates. The purpose of the tests was to establish data of cladding ballooning and burst with reference to LOCA conditions. As mentioned before, although the REBEKA tests were not originally included in FUMAC, BISON simulations are presented here for completeness and including a 3D analysis demonstration (Section 2.2.4) which is of potential interest to the project.

2.2.1 Description of the tests

The cladding tubes had a fabricated inner/outer diameter of 9.30/10.75 mm, with a 325 mm heated length, and were heated indirectly by conduction heating from the inside, using an electrically insulated heater rod. A stack of alumina annular pellets (Al_2O_3) was used to simulate the fuel column. The diametral clearance between the cladding inner diameter and the pellet outer diameter was 0.15 mm. The test parameters covered a range of 1 to 14 MPa for the internal rod (He) pressure and 1 to 30 K s^{-1} for the heating rate. The test atmosphere was almost stagnant steam at atmospheric pressure and at a temperature of 473 K. The cladding temperatures were measured by thermocouples spot-welded on the outer surface of the cladding. Schematics of the experimental setup and procedure are given in Fig. 2.8. More details on the experimental apparatus and conditions are given in [19,20,44].

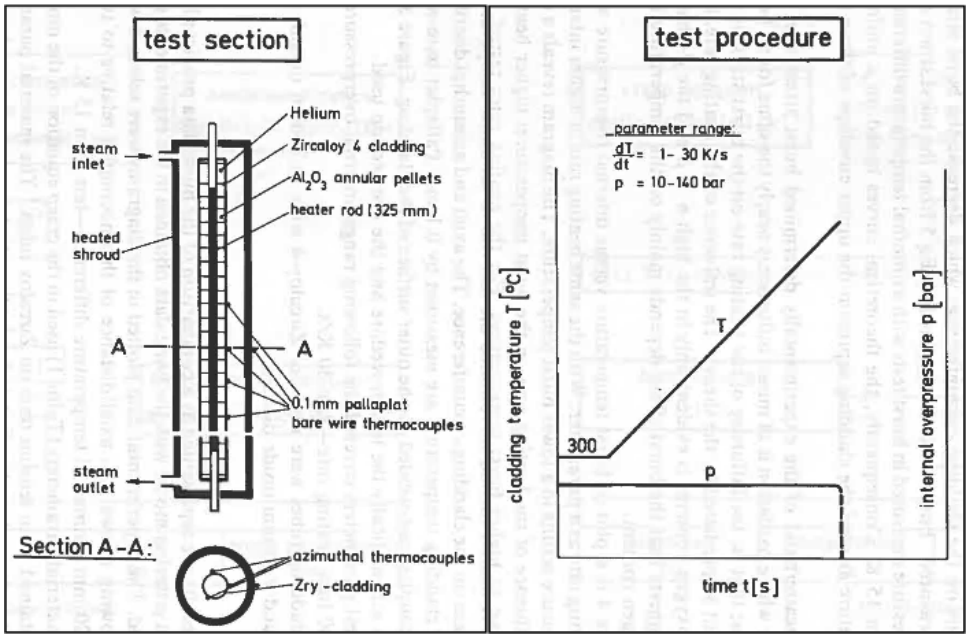

Figure 2.8: Schematics of the experimental setup (left) and procedure (right) for the REBEKA tests [19, 20,44].

2.2.2 Setup of BISON simulations

The considered cases are modeled considering only the cladding, while the alumina pellets are taken into account by imposing a proper temperature boundary condition at the cladding inner radius, which accounts for the heat transfer through the inner components. For simplicity, only the heated portion of the rods was simulated. In particular, the internal electric heating was simulated by a time-dependent Dirichlet temperature boundary condition applied to the tube inner wall and consistent with the experimental conditions. In particular, a parabolic temperature profile symmetric with respect to the tube mid-plane was considered, which results from the uniform axial power generation in the heater rod [44]. To estimate the temperature variation over the heated length of the cladding, simplified calculations of axial heat conduction within the rod and convection to the outer steam atmosphere were performed. Pressure equal to the experimental value was applied at the tube inner wall. A 2-dimensional axisymmetric quadratic (Quad8 elements) mesh was used to model the geometry of the considered rods. In addition, to investigate inherently three-dimensional aspects, such as the effect of azimuthal temperature differences, 3D simulations were conducted employing hexahedral elements (Hex20 elements). Taking advantage of the symmetry of the problem, only the lower half of the heated cladding length was modeled in the 2D simulations. For the 3D simulations, a quarter of the cladding circumference was modeled.

The combined overstress and plastic instability criterion for cladding burst failure (Section 1.4) was used for the REBEKA simulations.

2.2.3 Results

Using the 2D axisymmetric model, simulations were conducted of the REBEKA experiments with a heating rate of 1 K s^{-1}, considering the full range of 1 to 14 MPa for the internal cladding pressure. As for the 3D model, only one case is reported here, in order to demonstrate BISON's ability to assess the impact of azimuthal temperature variations on cladding ballooning and burst. The predictions of burst temperature at the various internal cladding pressures are compared to the available experimental data in Figure 2.9. The trend of increasing burst temperature with decreasing internal pressure is reproduced, and the quantitative accuracy of predictions is reasonable. Nevertheless, a moderate but systematic under-prediction is observed. Such discrepancies may be due to uncertainties inherent in the cladding mechanics, burst, oxidation and phase transformation modeling, three-dimensional effects (azimuthal temperature differences) that cannot be captured by 2D modeling.

Figure 2.10 shows contour plots of temperature, creep strain magnitude, and locations where the local stress reached the limiting burst stress for the case with 10 MPa internal pressure; results are shown at the time of cladding burst. The creep strain magnitude (-) is defined as

$$\varepsilon_{cr,mag} = \sqrt{\frac{2}{3}\,\overline{\overline{\varepsilon_{cr}}} : \overline{\overline{\varepsilon_{cr}}}} \tag{2.1}$$

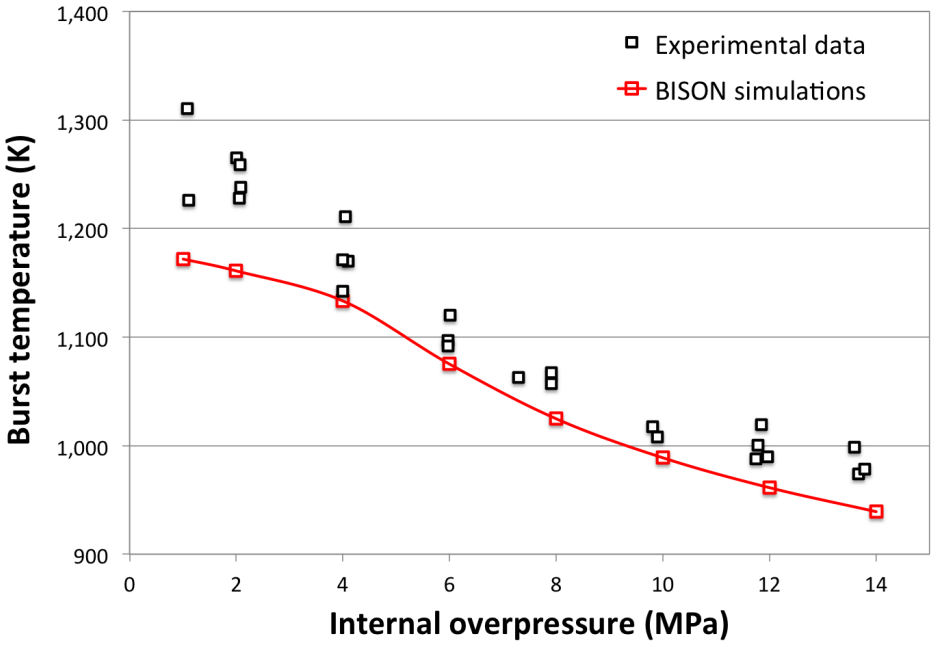

Figure 2.9: Comparison between BISON predictions and experimental data of cladding burst temperature for the simulations of the REBEKA tests with heating rate of 1 K s^{-1}.

where $\overline{\overline{\varepsilon_{cr}}}$ is the creep strain tensor. The cladding ballooning effect as reproduced by BISON is obvious. Cladding failure due to burst is predicted at a temperature of about 993 K and a creep strain magnitude of about 1.1, which reasonably conform to experimental observations [19,44]. The burst stress is first reached in the mid-section of the cladding, where the strain is largest. The time evolution of the hoop stress and burst stress in the cladding mid-section in proximity of time of burst are plotted in Figure 2.11. The corresponding hoop strain is also shown. The stress increases under the effect of the constant inner pressure as the cladding wall thins due to the large creep strain. The burst stress decreases over time due to increasing temperature and progressive cladding oxidation (and in general also due to phase transformation, not observed at the temperatures reached in this specific case). The calculated time evolution of the cladding hoop strain is consistent with the experimental observations [44].

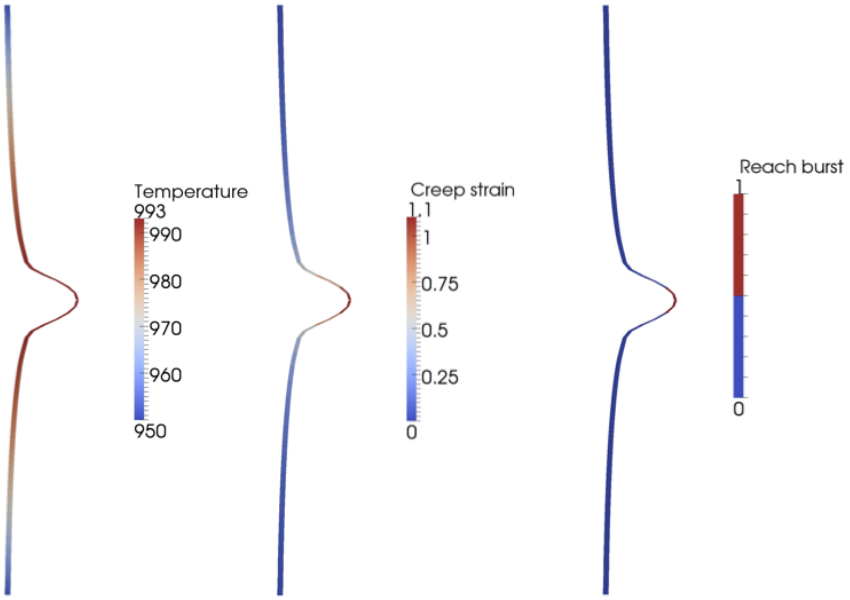

Figure 2.10: Contour plots for the BISON 2D simulation of the REBEKA test with 10 MPa internal pressure at the time of cladding burst. The results for the lower half of the heated cladding are mirrored to obtain a full-length view. The view is magnified 4 times in the radial direction for improved visualization.

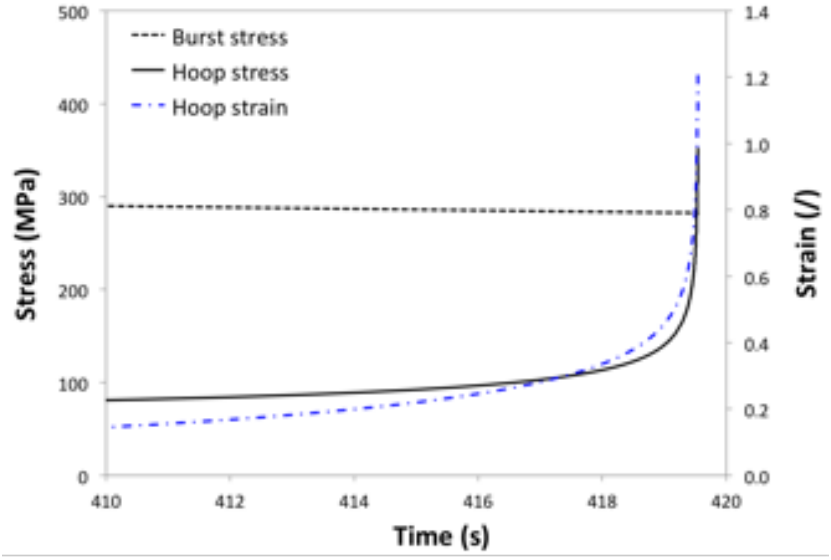

Figure 2.11: Time evolution of burst stress, hoop stress, and hoop strain at the cladding mid-section in proximity of time of burst. The results refer to the BISON simulation of the REBEKA test with 10 MPa internal pressure.

2.2.4 3D simulation

In addition to the above mentioned boundary conditions applied to the 2D simulations, in the 3D simulation an azimuthal temperature gradient was applied. A maximum azimuthal temperature variation of 30 K was considered, in conformity with the experimental indications from thermocouple measurements [20]. The results are presented for the exemplifying case of 10 MPa internal pressure at the time of cladding burst. Figure 2.12 shows contour plots of temperature, creep strain magnitude, and locations where the local stress reached the limiting burst stress. The 3D simulation reproduces the non-uniform cladding ballooning and a localized burst on the hottest side of the cladding, which is consistent with experimental observations [20]. Note that the predicted burst temperature is higher (by about 10 K) than for the corresponding 2D simulation, thus indicating that capturing 3D aspects such as the effect of azimuthal temperature differences is of importance for fuel analysis during LOCA accidents. Further investigation of 3D effects in fuel rod analysis during LOCAs with BISON will be pursued in the future.

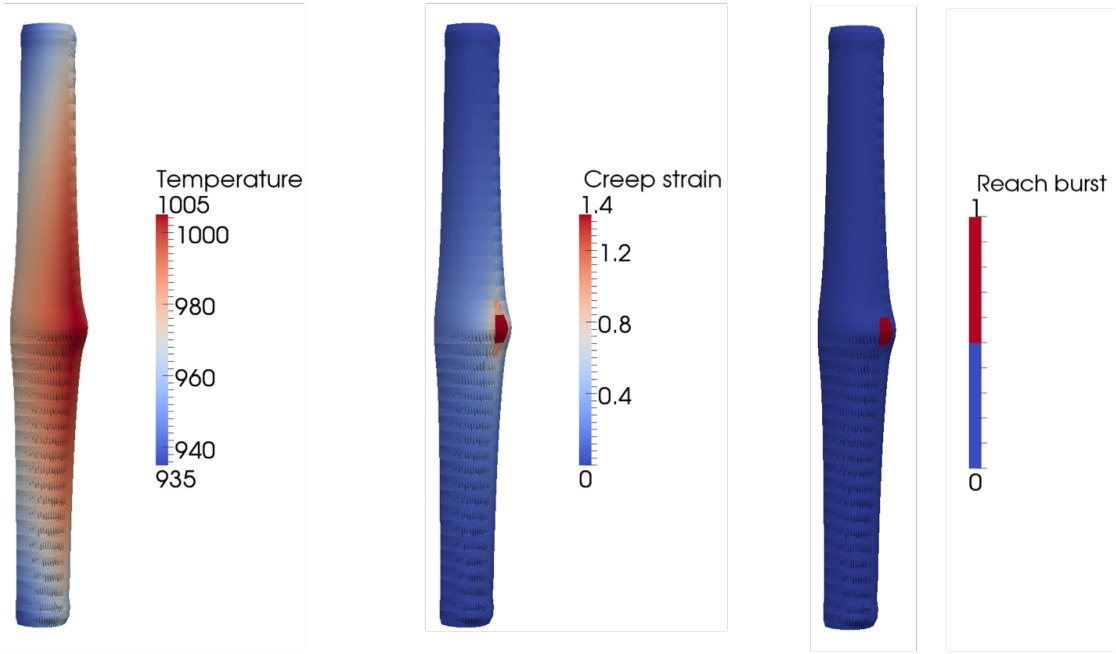

Figure 2.12: Contour plots for the BISON 3D simulation of the REBEKA test with 10 MPa internal pressure at the time of cladding burst. The results for the lower quarter of the heated cladding are mirrored to obtain a full-length, half circumference view. The view is magnified 3 times in the radial direction for improved visualization.

2.3 QUENCH-L1

BISON simulations for the QUENCH-L1 experiment [45] were carried out for rods 4 and 7. Test rods contain annular ZrO_2 pellets, with heating achieved using tantalum heaters within the pellets. Experimental data was used as much as possible to develop accurate boundary conditions for the simulations.

2.3.1 Test description

The QUENCH facility was constructed to investigate hydrogen release during reflood of an overheated reactor core. As illustrated in Figure 2.13, during the QUENCH-L1 test, superheated steam and argon enter a test rod bundle at the bottom of the assembly and flow upward. The argon, steam, and produced hydrogen (from the zirconium-steam reaction) exit through a water-cooled off-gas pipe to a condenser, separating steam from the argon and hydrogen. Quenching water is injected via an independent line at the bottom of the assembly.

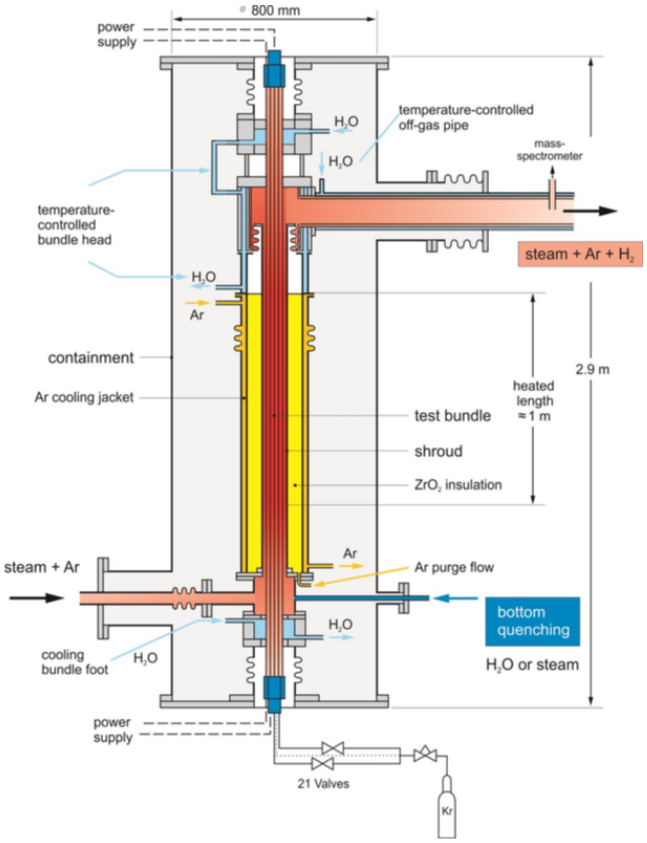

Figure 2.13: Test section with flow lines (Figure 4 from [45]).

The test bundle consists of 21 fuel rod simulators and four corner rods, as shown in Figure 2.14. A shroud surrounds the bundle to simulate the adiabatic surrounding of a reactor core as well as guide steam and gas through the assembly. Rods are divided into two groups, each connected to a separate DC generator in parallel: rods 1-9 and 15 were designated as internal rods while rods 10-14 and 16-21 were referred to as external rods.

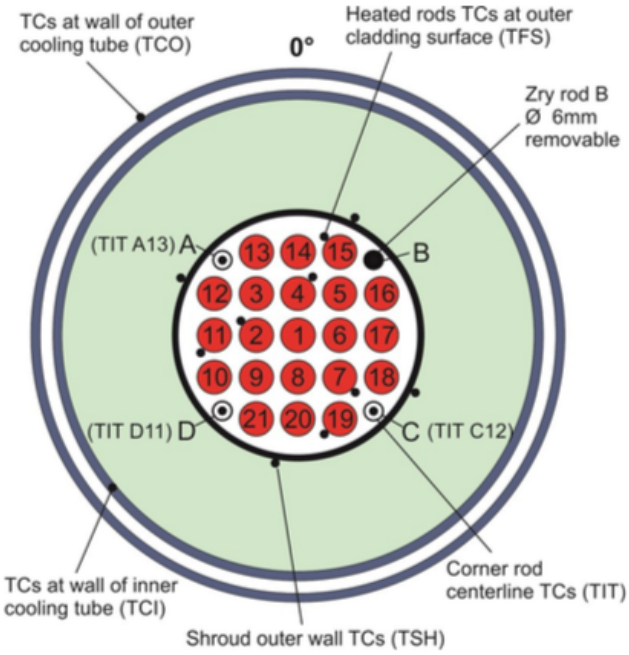

Figure 2.14: Thermocouple instrumentation and rod designation (top view) (Figure 12 from [45]).

Each fuel rod simulator is approximately 2.5 meters in length, as illustrated in Fig. 2.15. Various sealing and insulation plates as well as spacers provide support along the axial length of the rod. The heated length of the simulator is surrounded first by molybdenum electrodes then copper electrodes are located at the ends of the rod. The heated length of the rod begins at 692.5 mm from the bottom of the rod. It consists of a central tantalum heater with a diameter of 6 mm surrounded by 1.575 mm thick ZrO_2 pellets. The plenum separating the heater/pellet combination meant to simulate fuel pellets is filled with krypton gas with a gap between the outer radius of the ZrO_2 pellets and the cladding of 0.075 mm. The Zircaloy-4 clad of 0.725 mm thickness encases this system. The heated length is 1024 mm long.

Suffice it to say, at this point, that there are myriad system components, structural and electrical support elements in the fuel rod simulators, and instrumentation throughout this experimental setup, but as data collected from the fuel rod simulators is of principle interest to computational modeling efforts, experiment behavior is the focus of the remaining description. Thermocouples along the surface at axial locations ranging from -250 mm to 1250 mm in increments of 100 mm as well as those in the plenum of instrumented rods collect temperature data throughout the

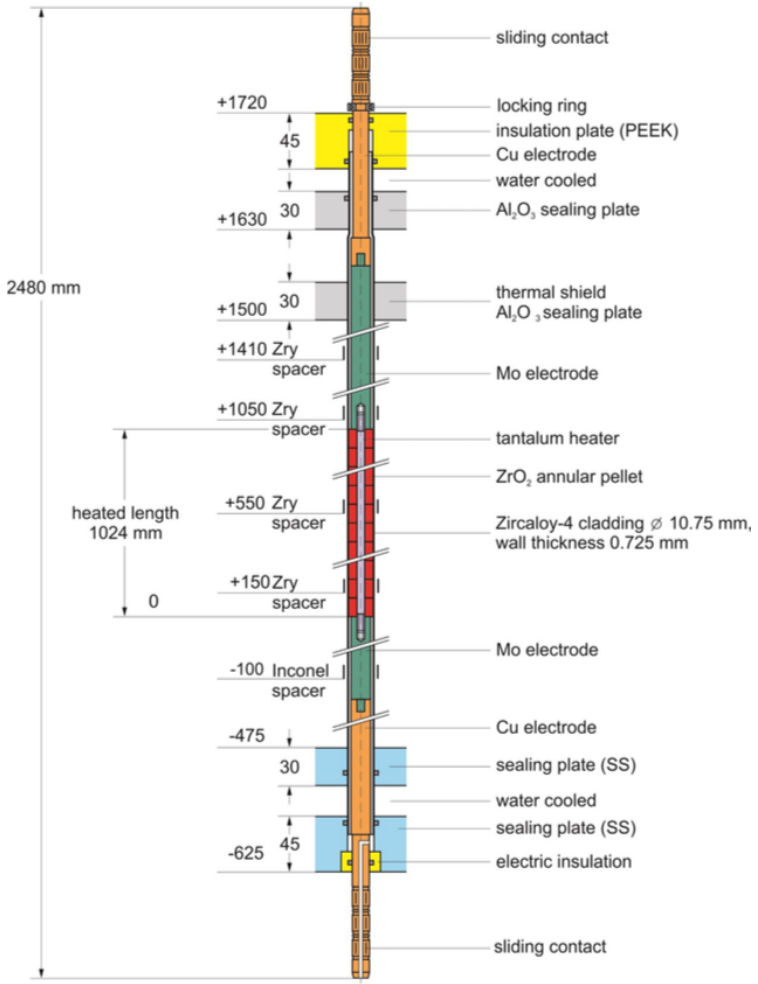

Figure 2.15: Cross section of a fuel rod simulator (Figure 6 from [45]).

experiment with no failed TMs detected at the conclusion of operations. Pressure sensors in the plenum as well as the inlet and outlet record internal rod and system pressures respectively.

As shown in Figs. 2.16 and 2.17, the experiment began by applying a total power of 3.5 kW to the electrical bundle. Fuel rod simulators were then individually backfilled to 55 bar and electrical power was rapidly increased to 43 kW to initiate the transient. This initial power increase was followed by a steady increase to 59 kW over the next 87 seconds. The power was then rapidly decreased back to 3.5 kW with water injection at a rate of 100 g/s beginning at 207 s. The quench progressed toward the top of the coolant channel (bundle bottom @ 246 s, ballooned region @ 266s, whole bundle @ 293 s).

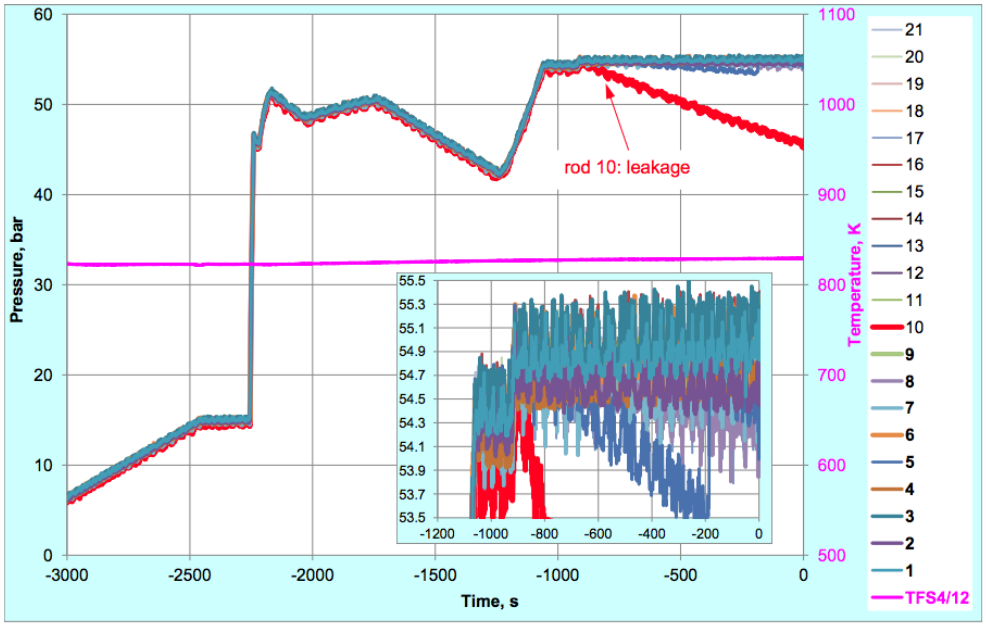

Figure 2.16: Rod pressurization process (Figure 9 from [45]).

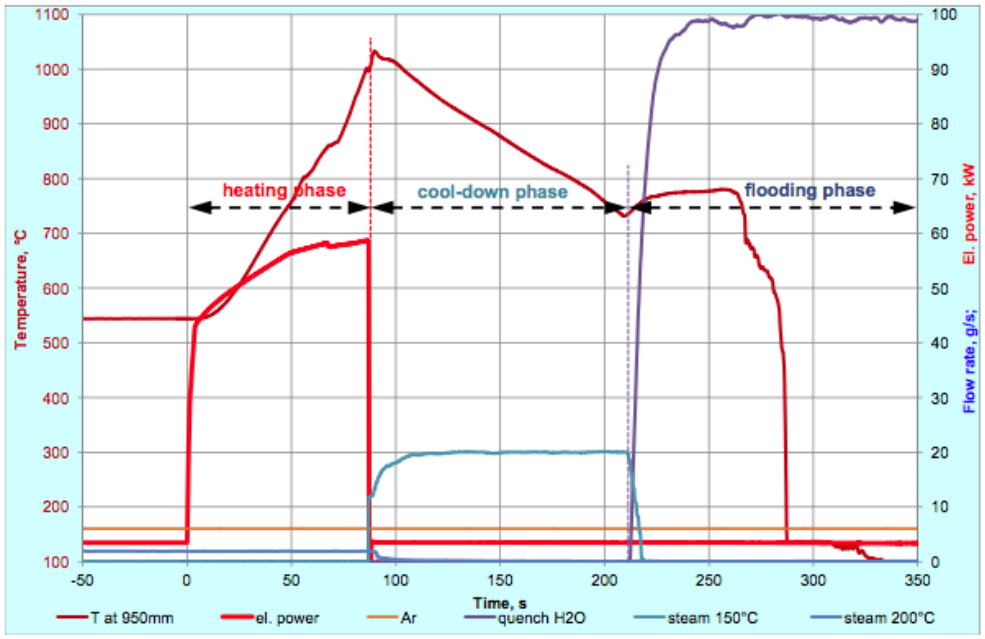

Figure 2.17: Test scenario (Figure 16 from [45]).

2.3.2 Setup of BISON simulation

Rods 4 and 7 were chosen for consideration since they had the largest number of axial thermocouples. Results from the instrumentation were used as applicable to define boundary conditions in the model. The aim of the calculation was to simulate the fuel rod behavior up to burst and compare to measured burst conditions. As such, a terminator was set up to end the simulation upon detecting a burst in the model.

2.3.2.1 Mesh Development

A 2D, axisymmetric, QUAD4 finite element mesh was developed considering only the headed portion of the rods. As illustrated in Fig. 2.18, the heater and pellet blocks fairly approximate their experimental counterparts as the Ta heater is a solid cylindrical bar, and the ZrO_2 pellets are hollow cylindrical pellets fitting closely around the heater with little space between them. They are modeled as two separate blocks with material properties of the ZrO_2 pellets obtained from [45]. Zircaloy-4 material models implemented in BISON provide thermal and mechanical properties for this block.

2.3.2.2 Boundary Condition Development

Data from the experiment now needs to be formatted in a way that BISON can use as boundary conditions. Provided instrument data begins at -100.6 s before the initial power ramp begins the transient, but a ramp of temperature and pressure for the system initial conditions is necessary. In addition, the pressure ramp illustrated in Figure 2.16 begins well before -100.6 s so is digitized directly from the plot to provide accurate plenum conditions. Boundary conditions on the outside of the cladding depend upon axial position and must be interpolated in a way that both preserves the original data but predicts the data shape accurately between experiment collection points as BISON linearly interpolates between provided data points. This very likely provides an unrealistic shape (especially in the case of temperatures); so other interpolation or statistical fitting methods are employed.

To provide heat to the system, a heat source must be specified. In the majority of BISON simulations, this is a fission source from whatever fuel type is being modeled, but this experiment utilizes tantalum heaters instead. Power provided to the inner and outer rod groups over the course of the experiment is detailed in the collected data and is kept generally the same (3.5 kW total) before the transient occurs. A ramp from zero power is included before the pressure ramp in Figure 2.16 to stabilize the system. This ramp, along with the recorded power, is read into the input as a function, and applied as a heat source. The heat source kernel requires the power function to be volumetric (W/m^3), so dividing the total power to inner rods by the number of rods and volume of each heater yields the necessary boundary condition data.

The plenum pressure boundary condition requires a bit more conditioning. The gas gap pressure is given from -100.6 s through rod bursts and subsequent quenching, but the initial rod backfill

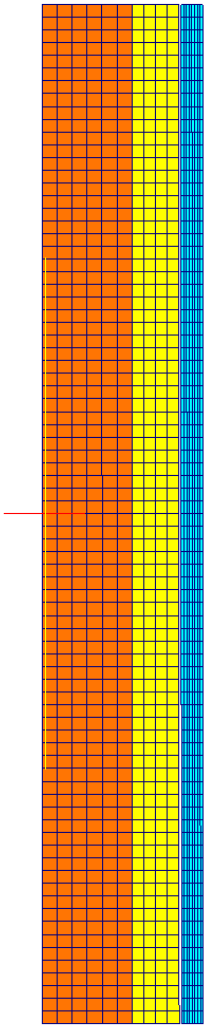

Figure 2.18: Computational mesh with different materials specified (radial dimension scaled 20x) [orange: Ta heater, yellow: ZrO_2 pellets, blue: Zry-4]

data is only provided in Figure 2.16. This figure is digitized, and obtained values are used as the internal pressure boundary condition from approximately -3000 s to -911 s at which point the pressure recorded for each rod at -100.6 s is held steady.

This boundary condition now extends from the beginning of the simulation through the region of interest for this modeling effort. The sudden drop in pressure for each rod at around 50 s indicates the point at which the cladding fails via the burst mechanism. Informing the simulation from experimental pressure data is problematic around this point, as BISON typically predicts later burst times for this problem. Providing the experiment pressure values to the simulation in cases where BISONs burst time prediction is later than experiment burst time reduces the

pressure on the cladding prematurely, and it becomes less likely that the simulated fuel will burst due to reduced cladding stresses. This sudden drop in plenum pressure causes the simulation to depart from conditions leading to a burst.

To address this, pressures from the beginning of the transient until the burst are fitted to a linear regression model, and this pressure model is used as the plenum pressure boundary condition from t = 0 s until burst. Employing this modeling scheme does remove perturbations that can contribute to triggering cladding burst and the larger the difference between experimental and simulation burst times, the more the model departs from collected data, but this is viewed as the most viable method to predict extended plenum pressure behavior as the models difference between collected data up until the burst is minimal.

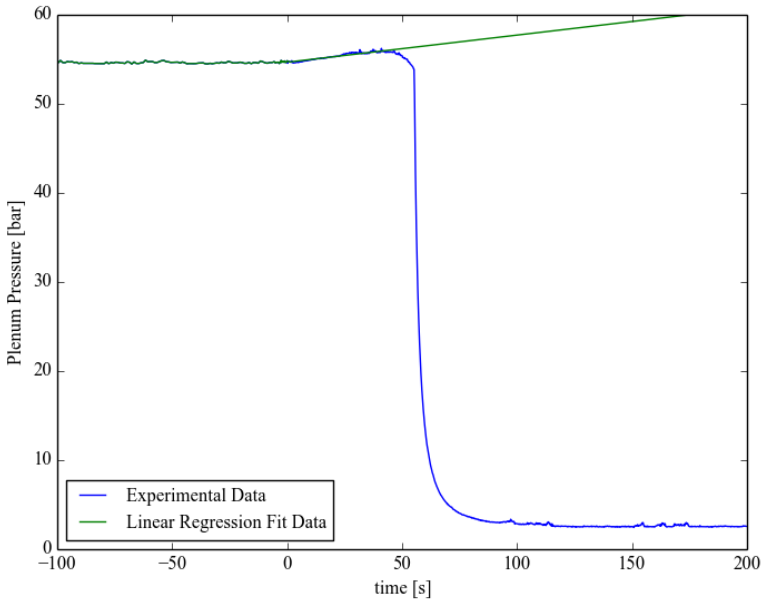

Figure 2.19: Plot of plenum pressure vs. time for Rod 4.

The most involved data conditioning is for the outer cladding temperature boundary condition. Typically, a BISON simulation would either utilize the included coolant channel model or be coupled to a system thermal hydraulics code to provide the outer temperature and flow conditions, but to obtain results accurate to experimental conditions for individual fuel rod simulators, the sampled cladding surface thermocouple data is conditioned. Many rods in the experiment do not have thermocouples along the entire heated length (which, again, is why rods 4 and 7 were chosen). Even data from rods with most of the heated length instrumented are sparsely sampled (TM at every 100 mm); so some features of the axial temperature distribution were not collected. Providing the axial temperatures as is would cause BISON to linearly interpolate temperatures for outer nodes between axial positions with thermocouple collection points, yielding unrealistic temperature distributions in this sparsely sampled case.

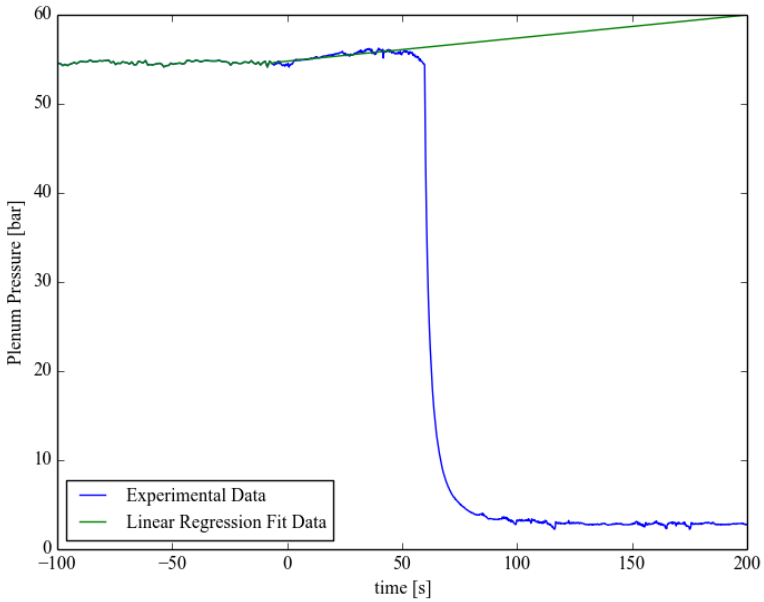

Figure 2.20: Plot of plenum pressure vs. time for Rod 7.

Two options for determining outer cladding temperature values come to mind: fitting statistical models to the data or interpolation techniques. The sparse sampling makes fitting an unattractive choice as statistical modeling relies upon a wealth of input data to accurately predict the behavior of a quantity of interest. However, using cubic spline interpolation with the temperature data will exactly provide data at collection points with a temperature distribution with more realistic features than linear interpolation.

While this is a promising method for providing more detailed boundary conditions to the BISON models from this sparse data set, values to interpolate between are still necessary. Rod 7 has the axial collection points required, but the lowest collection point for rod 4 is at 25 mm while the bottom of the simulated fuel rod begins at 0 mm. To remedy this gap in the data, we assume system conditions are likely to be similar before flowing past the heated length of the fuel rod simulators, and data from one thermocouple recording temperatures from below the heated length of rod 7 is added to the rod 4 data.

The data, as well as interpolated values, are plotted in Figures 2.21 and 2.22 at several points during the transient power ramp. Comparing the interpolated profiles of the temperature distributions for rods 4 and 7 throughout the transient, rod 7 has a more centrally located peak temperature. It also appears that the interpolated lower axial location rod 4 values may be missing a local temperature decrease around 150 mm in elevation as this is evidenced in the rod 7 profiles, but otherwise the profiles are quite similar. The interpolated outer temperature values are provided as a piecewise bilinear function to the BISON simulation.

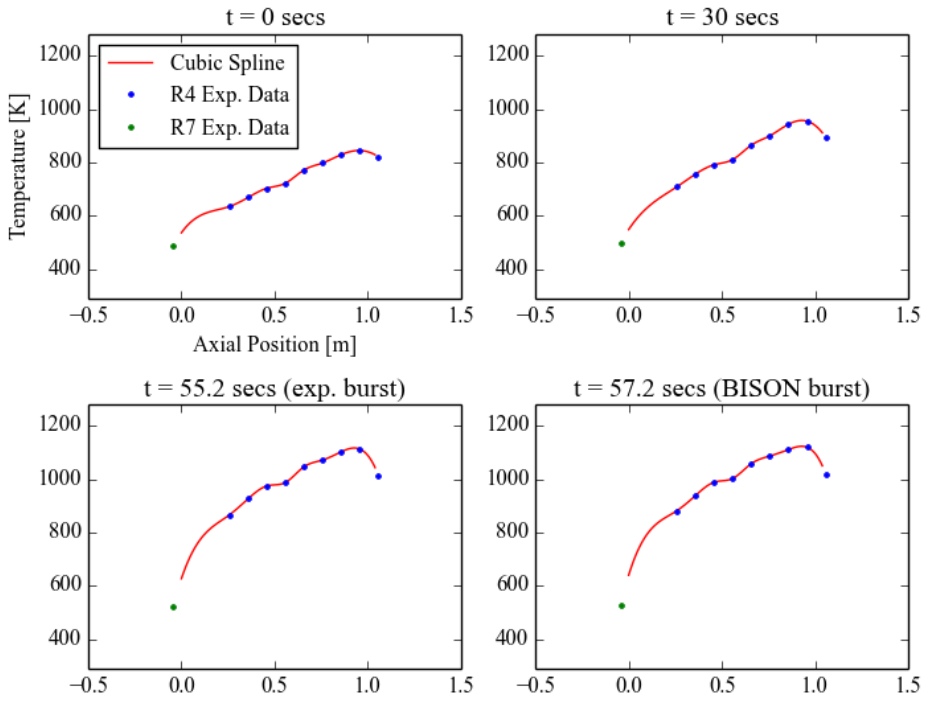

Figure 2.21: Rod 4 Temperature vs. axial location on outside of clad.

The final boundary condition the simulation requires is the system pressure along the cladding. Pressures are collected from the inlet and outlet of the cooling loop and values recorded over time are given in [45]). Pressure along the heated length is linearly interpolated as the pressure condition along the heated length. This condition would not be linear in the experiment, however. A more in-depth future study would feature development of a more cosinusoidal shaped pressure boundary condition between the inlet and outlet.

2.3.3 Results

The BISON simulation of the QUENCH-L1 test is meant to replicate experiment conditions as closely as possible utilizing the provided data from the initial pressurization and temperature increase phases until fuel failure. Cladding temperature drives the thermally activated processes of cladding creep and ballooning, which ultimately leads to cladding burst. Thus, accurate determination of the temperature conditions throughout the system is a prerequisite for realistic fuel performance simulation results.

Ballooning occurs when the cladding strain rapidly accelerates with increasing temperature during the last approximately 25 s before burst. As Zircaloy cladding creep is exponentially depen-

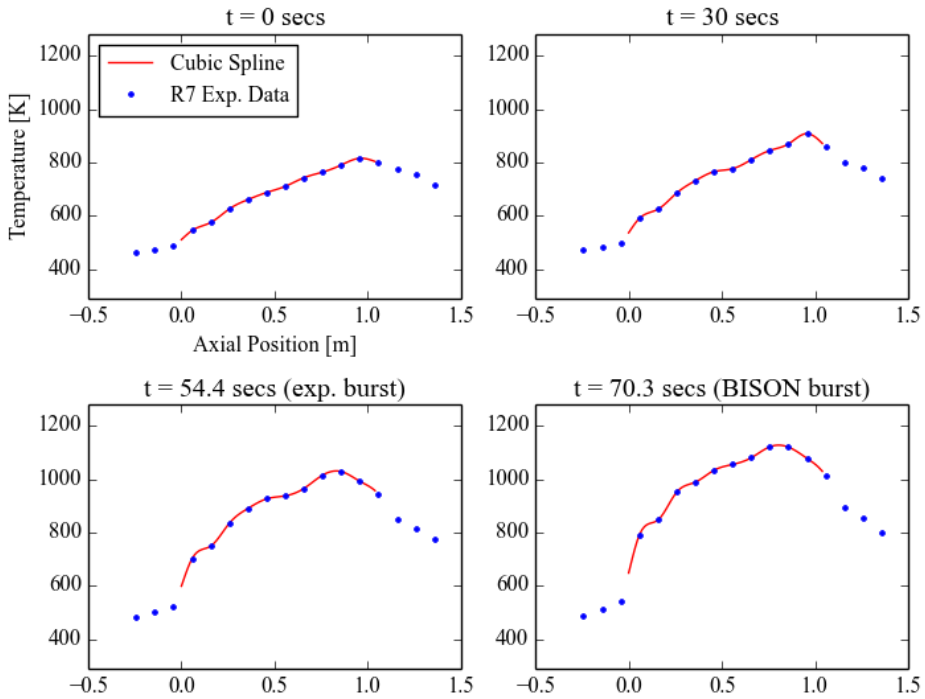

Figure 2.22: Rod 7 Temperature vs. axial location on outside of clad.

dent upon temperature, the behavior observed is qualitatively consistent, and BISON reproduces cladding ballooning relatively well during the LOCA test. Rapid thermal creep and ballooning continue until failure due to burst at the location of maximum strain. BISON predicts cladding burst failure according to the plastic instability criterion as strain rate reaches the limit level.

Comparison of metrics between the experiment and calculated models are provided in Tables 2.3 and 2.4. Cladding burst is predicted to occur at 55.8 and 68.4 s after beginning the transient heating phase for rods 4 and 7, respectively. Both times are slightly later than the experimental failures observed at 55.2 and 54.4 s. The hoop strain is underpredicted in both cases by about a factor of 3. Temperature and pressure calculations are very close to the measured values at the time of failure. Both predicted burst elevations are higher than the experimental locations but are consistent with the experiment in that burst elevation occurs at the upper end of the fuel rod simulators.

Table 2.3: Rod 4 Experiment and Simulation Results

	Experiment	BISON
Burst Time [s]	55.2	55.8
Burst Elevation [mm]	979	927
Plenum Burst Pressure [bar]	53.9	56.4
T @ 950 mm [K]	1154	1117
Strain [%]	28.9	8.9
Max Diameter [mm]	15	11.6
Min Diameter [mm]	13	10.8

Table 2.4: Rod 7 Experiment and Simulation Results

	Experiment	BISON
Burst Time [s]	54.4	68.4
Burst Elevation [mm]	953	800
Plenum Burst Pressure [bar]	55.1	56.6
T @ 950 mm [K]	1074	1077
Strain [%]	24.8	8.1
Max Diameter [mm]	14.7	11.5
Min Diameter [mm]	12.5	10.8

2.4 Halden test IFA-650.2

LOCA tests at Halden (IFA-650 series) are integral in-pile single rod tests. Relative to separate effects tests, they also provide information on the integral behavior of a fuel rod during a LOCA accident. The second trial test run IFA-650.2 [46] was performed in May 2004.

2.4.1 Test description

The test was carried out using a fresh, pressurized PWR rod and low fission power to achieve the desired temperature conditions. The rod plenum volume was made relatively large to be able to maintain stable pressure conditions during ballooning. The fabrication characteristics of the IFA-650.2 fuel rod are reported in Table 2.5.

The fuel rod was located in a standard high-pressure flask in the IFA-650 test rig in the Halden reactor. A heater surrounding the rod was used to simulate the heat from adjacent rods. The flask was connected to a high-pressure heavy water loop and a blowdown system. During normal operation prior to the LOCA test, the rig was connected to the loop and forced circulation flow conditions existed. Then, the rig was disconnected. A natural convection phase began, with water flowing up between the fuel rod and flow separator (with heater) and down between flow separator and flask wall. Full pressure still existed in the rig. LOCA was initiated by opening the valves leading to the blowdown tank (blowdown phase). The initial pressure in the loop was $\sim$7 MPa and the counterpressure in the blowdown tank was $\sim$0.2 MPa. The channel pressure decreased to 3-4 bars, and the rig was practically emptied of water within 30-40 seconds. Stagnant superheated steam surrounding the rod provided inadequate cooling and the cladding temperature increased quickly (heat-up phase). A low fission power of 2.3 kW/m was used to simulate decay heat and achieve the desired temperature conditions. Cladding ballooning and

Table 2.5: Design data of IFA-650.2 fuel rod [46]

Fuel material		UO_2
Fuel density	%TD	95.0
^{235}U enrichment	wt%	2.0
Active stack length	mm	500
Pellet OD	mm	8.29
Pellet ID	mm	0
Cladding material		Zy-4
Cladding ID	mm	8.36
Cladding OD	mm	9.50
Diametral gap	μm	70
Free volume	cm^3	17.4
Fill gas		He
Fill gas pressure	MPa	4.0

burst rupture occurred during the heat up phase. measured cladding temperature at burst was $\sim$815°C. The test was ended by a reactor scram.

2.4.2 Setup of BISON simulation

The rod geometry was modeled following the design specifications from [46] (Table 2.5). The enriched fuel pellet column was represented with a smeared fuel column. Natural UO_2 pellets at the top and bottom of the fuel stack were also included. A single rod upper plenum was considered, whose volume is the sum of the various plenum volumes in the more complex real geometry [46]. A 2-dimensional axi-symmetric quadratic (Quad8 elements) finite element mesh was used. The enriched fuel column mesh consisted of 6 radial elements and 62 axial elements. Each natural UO_2 pellet mesh consisted of 6 radial elements and 1 axial element. The cladding mesh consisted of 256 axial elements and 3 radial elements.

The combined overstress and plastic instability criterion for cladding burst failure (Section 1.4) was used for the IFA-650.2 simulation.

The boundary conditions (BCs) in terms of linear heat rate and rig pressure were derived from the raw data from provided by the Halden Project and tabulated for usage in BISON. Temperature BCs at the cladding outer surface were evaluated based on cladding outer temperatures which were measured at two axial positions during the experiment, and were also part of the Halden data. In particular, axial temperature profiles at the clad outer surface were obtained using some simplifying assumptions and imposing coincidence with the measured temperatures at measurement axial locations. The obtained profiles were used as outer cladding temperature BCs in absence of detailed thermal-hydraulics calculations. The procedure and assumptions adopted for the calculation of the temperature BCs used for the BISON simulations of IFA-650.2 at INL was first discussed on the FUMAC website in advance of the RCM2 [47]. A detailed description is given hereinafter.

2.4.3 Determination of the temperature boundary conditions

Clad outer temperature axial profiles are obtained based on the following assumptions:

- The effect of radiation is lumped into an 'effective' heat transfer coefficient. This is based on linearizing the radiative heat transfer law, $q'' \propto \left(T_1^4 - T_2^4\right)$, into $q'' \propto h_{rad}\,(T_1 - T_2)$, where q'' is the heat flux and $h_{rad} \propto T^3_{average}$ and has units of a heat transfer coefficient. The linearized equation is accurate if T_1 and T_2 are close enough. Under this assumption, the axial clad temperature profile can be written in a form as if heat transfer was purely convective

$$T(z) = T_{cool}(z) + q''(z)/h_{eff}(z) \tag{2.2}$$

  where z is the axial coordinate, $T_{cool}(z)$ is the coolant temperature, and h_{eff} is the 'effective' heat transfer coefficient (convection+radiation).

- The coolant temperature is approximated as the heater temperature at the axial position z. This is estimated based on the Halden data of measured heater temperature at two axial location and a linear interpolation.
- The heat flux is proportional to the local linear heat rate, i.e., $q''(z) \propto q'(z)$. This is reasonable provided that the coolant channel conditions are reasonably uniform along the rod and that no axial fuel relocation takes place during the test. From this assumption and Eq. 2.2, it follows:

  $$T(z) = T_{cool}(z) + q'(z)/h^*(z) \tag{2.3}$$

  Where $h^*(z) = kh_{eff}(z)$ and k is a constant. The local linear heat rate, $q'(z)$, is obtained from the Halden data.
- $h^*(z)$ is determined based on the measured cladding temperatures. For this purpose, h^* is assumed to vary linearly along z

  $$h^* = Az + B \tag{2.4}$$

  The two equations needed to determine the coefficients A and B are the conditions of $T(z)$ (Eq. 2.3) being equal to the measured temperatures at the two measurement locations (thermocouples at clad outer wall).

The strongest simplification in the above approach is taking a linear fit of the heat transfer coefficient along the axial direction. When radiation is dominant, approximately $h^* \propto T^3_{average}$, which likely has a maximum at peak power position. However, the above approach based on measured temperatures may be accurate enough in view of the uncertainties involved in determining thermal-hydraulic boundary conditions.

Figures 2.23 to 2.26 show examples of estimated clad outer temperature profiles at selected instants during different phases of the experiment. Using the measured temperatures and an axially varying heat transfer coefficient, actually, allows one to capture effects such as the higher temperature in the lower part of the rod during the blowdown phase, which are difficult to explain [46] or reproduce through thermal-hydraulics calculations.

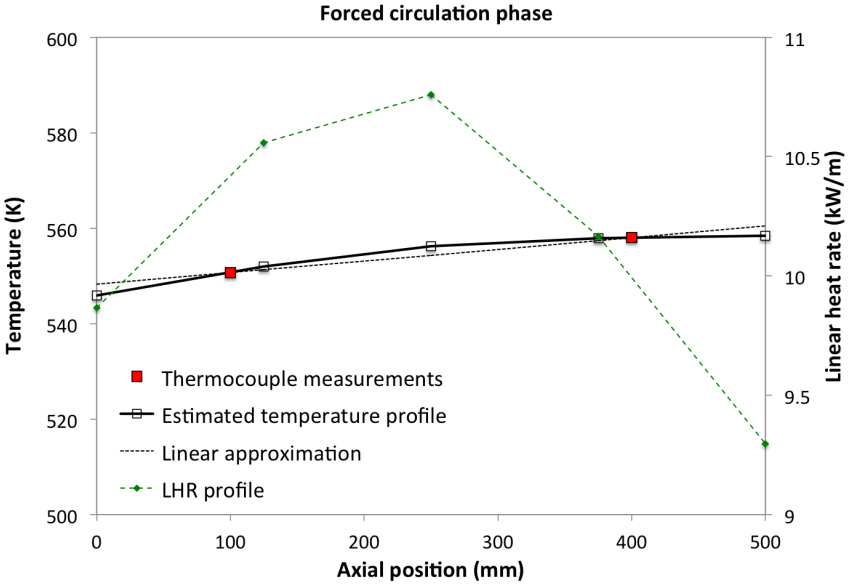

Figure 2.23: Estimated axial temperature profile at cladding outer surface at an instant during the forced circulation phase of the IFA-650.2 experiment. The measured temperatures at the thermocouple locations and the linear heat rate (LHR) profile interpolated from Halden data are also shown.

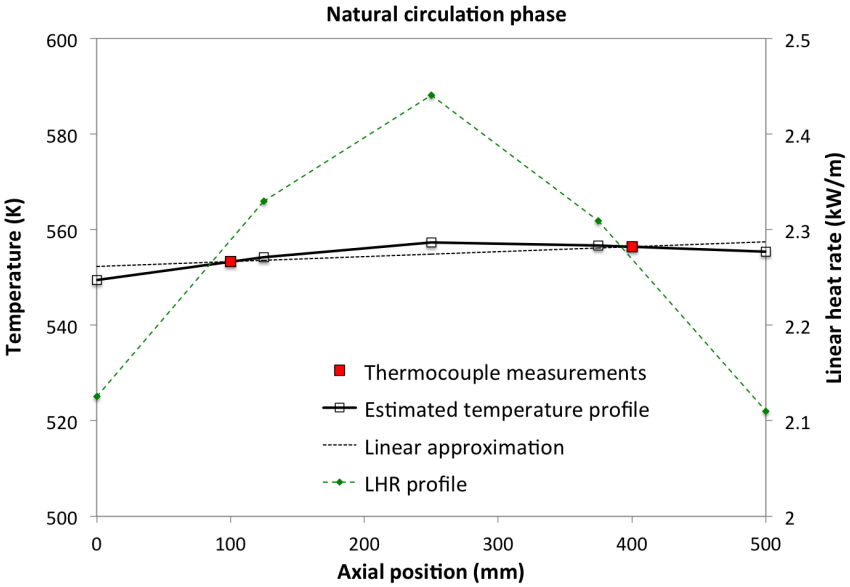

Figure 2.24: Estimated axial temperature profile at cladding outer surface at an instant during the natural circulation phase of the IFA-650.2 experiment. The measured temperatures at the thermocouple locations and the linear heat rate (LHR) profile interpolated from Halden data are also shown.

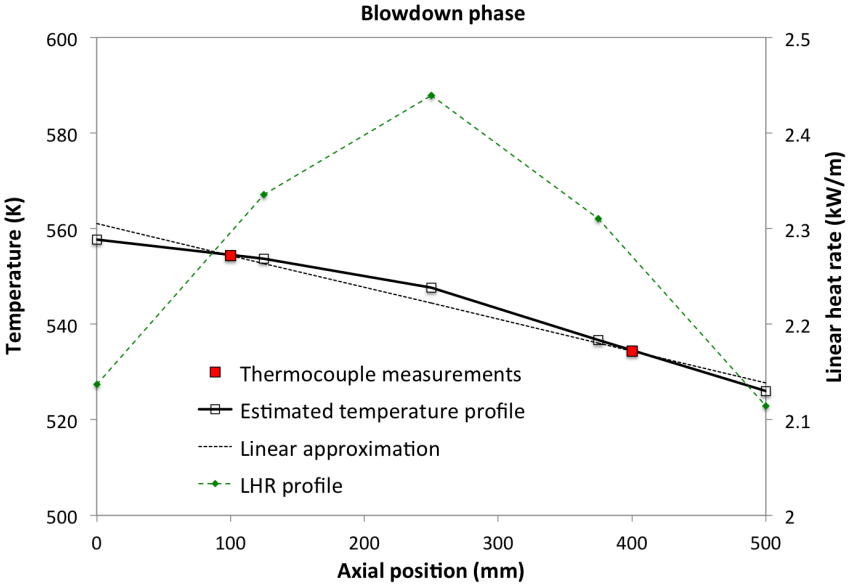

Figure 2.25: Estimated axial temperature profile at cladding outer surface at an instant during the blow-down phase of the IFA-650.2 experiment. The measured temperatures at the thermocouple locations and the linear heat rate (LHR) profile interpolated from Halden data are also shown.

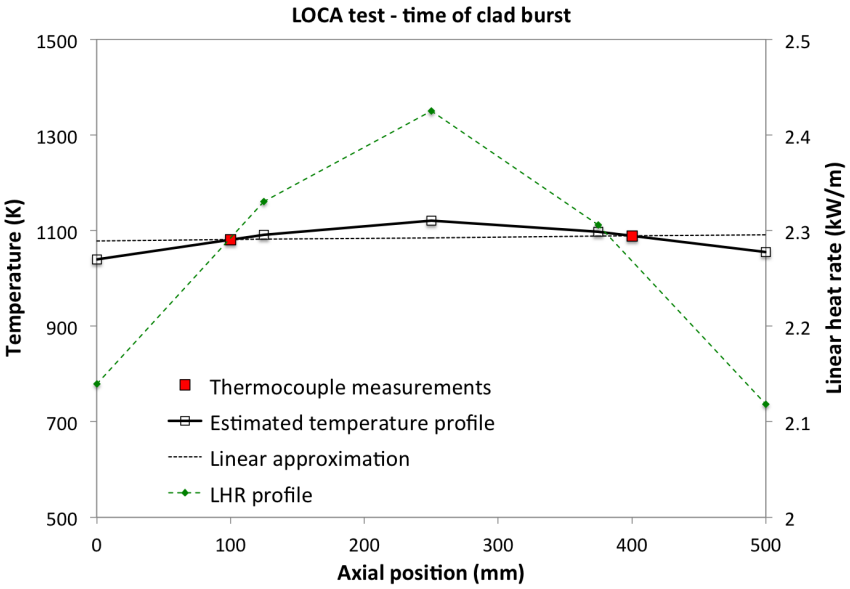

Figure 2.26: Estimated axial temperature profile at cladding outer surface at the time of cladding burst for the IFA-650.2 experiment. The measured temperatures at the thermocouple locations and the linear heat rate (LHR) profile interpolated from Halden data are also shown.

2.4.4 Results

In Figure 2.27, calculated inner pin pressure during the LOCA transient is compared to the on-line experimental measurement, with predicted and experimental time to burst being also illustrated. The comparison points out that both quantities are reasonably well predicted by BISON. Rod pressure is slightly over-predicted during the heat-up phase of the test, which may be ascribed to discrepancies in the calculated plenum temperature and/or evolution of fuel rod inner volume during ballooning.

In this work, cladding temperature boundary conditions are determined based off the measured cladding outer temperatures (Section 2.4.3). Clearly, temperature BCs at the cladding also affect plenum temperature and in turn, plenum pressure. The small 'dip' in the calculated pressure shown in Figure 2.27 at a time of around 30 s is due to a corresponding dip in the measured cladding outer temperatures (in particular, from the thermocouples at the upper axial position) from the Halden data. This behavior will require further investigation.

Fission gas release is very low due to the test being performed with a fresh fuel rod and is not expected to affect rod pressure significantly.

Calculated time to burst is ~91.1 s after the beginning of blowdown, i.e., about 7 s before the experimental time to burst (~98.5 s after the beginning of blowdown). Such an accuracy of the cladding burst prediction is encouraging.

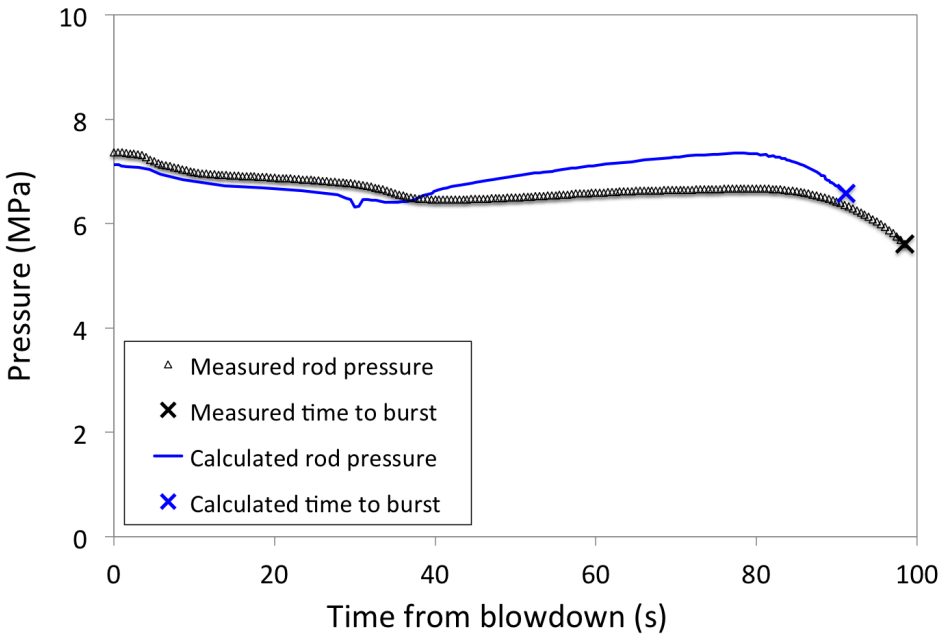

Figure 2.27: Comparison between measured and calculated fuel rod inner pressure and time to cladding bust for the Halden IFA-650.2 test. Time zero corresponds to the beginning of the blowdown phase.

2.5 Halden test IFA-650.10

The FUMAC priority case Halden IFA-650.10 has been simulated with BISON. The developed BISON computational model included a 2D geometric representation of the IFA-650.10 rod, consistent with the design specifications provided by the Halden Project, power histories and coolant conditions from the beginning of life through the commercial base irradiation and the LOCA test. Furthermore, the simulation was informed with the thermal boundary conditions calculated with the SOCRAT code and provided through FUMAC [48]. We exercised this computational model to obtain a BISON simulation of IFA-650.10 through all of the multiple phases of the experiment and to completion at the time of cladding burst failure.

Section 2.5.1 provides a description of the IFA-650.10 experiment. Section 2.5.2 describes the BISON computational model. Section 2.5.3 gives an account of how the boundary conditions for the different phases of the experiment were determined and supplied to BISON. Section 2.5.4 presents the simulation results and discusses the comparison of BISON predictions to the experimental data.

2.5.1 Test description

The tenth Halden LOCA test, i.e., IFA-650.10 [49], was carried out using a segment of a PWR rod that had been irradiated in a commercial PWR (Gravelines 5, 900 MWe, EDF, France) up to a burn-up of 61 MWd/kgU. During the test a low fission power (25 W/cm) was used to achieve the desired conditions for high cladding temperatures, ballooning and oxidation. A heater surrounding the rod and operating at 12 W/cm was used for simulating the heat from adjacent rods. The average cladding temperature increase rate during the heat-up was around 8 K/s. Cladding failure occurred ~249 seconds after blowdown at a cladding temperature of ~1025 K.

2.5.1.1 Fuel rod characteristics and experimental setup

The fabrication characteristics of the IFA-650.10 fuel rod are reported in Table 2.6. The test rod was a segment from the commercially irradiated PWR mother rod. The fuel and cladding materials are UO_2 and Zircaloy-4, respectively, with typical PWR design specifications. The refabricated rod was filled with a gas mixture of 95 % argon and 5 % helium at 4 MPa. Argon was chosen to simulate the (low-conductivity) fission gases. The rod plenum volume (free gas volume) was made relatively large in order to maintain stable pressure conditions until cladding burst occurred. The total free gas volume (17 cm^3) was thus practically all located in the plenum, outside the heated region.

The fuel rod was located in a standard high-pressure flask in the IFA-650 test rig, which was connected to a high-pressure heavy water loop and a blowdown system. A schematic of the test rig with its instrumentation is shown in Fig. 2.28 and a cross-sectional view of the rig is shown in Figure 2.29.

Table 2.6: Design data of IFA-650.10 fuel rod [49,50]

Fuel material		UO_2
Fuel density	%TD	95.32
^{235}U enrichment	wt%	4.487
Active fuel length	mm	440
Pellet OD	mm	8.21*
Pellet ID	mm	0
Pellet length	mm	10
Cladding material		Zy-4
Cladding ID	mm	8.36
Cladding OD	mm	9.50
Diametral gap	μm	150
Free volume	cm^3	17
Fill gas		Ar (95%), He (5%)
Fill gas pressure	MPa	4.0
Coolant temperature	K	508
Coolant pressure	MPa	7

* For consistency with the fuel-cladding diametral gap width [49,50].

The rod was located in the center of the rig and surrounded by an electrical heater inside the flask. The heater is part of a flow separator, which divides the space into a central channel surrounding the fuel rod and an outer annulus. The heater is used for simulating heat from the adjacent fuel rods in a power reactor core. Cladding temperature is influenced by both rod and heater powers. The flask was surrounded by a shroud and was placed inside the Halden reactor. The annulus between the shroud and the flask is filled with moderator (heavy water) at a pressure of 34 bar and a temperature of 235 C. One cladding surface thermocouple, TCC1, was located 9.5 cm above the fuel stack bottom, and the other two, TCC2 and TCC3, were attached 8 cm below the top of the stack. In IFA-650.10 the temperature of the heater was measured by two embedded thermocouples, i.e., TCH1 at the same elevation as TCC1, and TCH2 at ~2.6 cm below the fuel mid plane. A third thermocouple was placed on the outside surface at the axial midplane of the plenum. The axial power distribution was measured by three self-powered vanadium neutron detectors (ND) at three different elevations. The rig instrumentation also included a fuel pressure sensor (PF) and thermocouples at the inlet (TI) and outlet (TO) of the rig to measure the coolant temperatures.

2.5.1.2 Operation procedure and conditions

The experimental procedure for the IFA-650.10 test is detailed below [49]. Note that we refer here to the LOCA test performed in the Halden reactor on the pre-irradiated, refabricated PWR

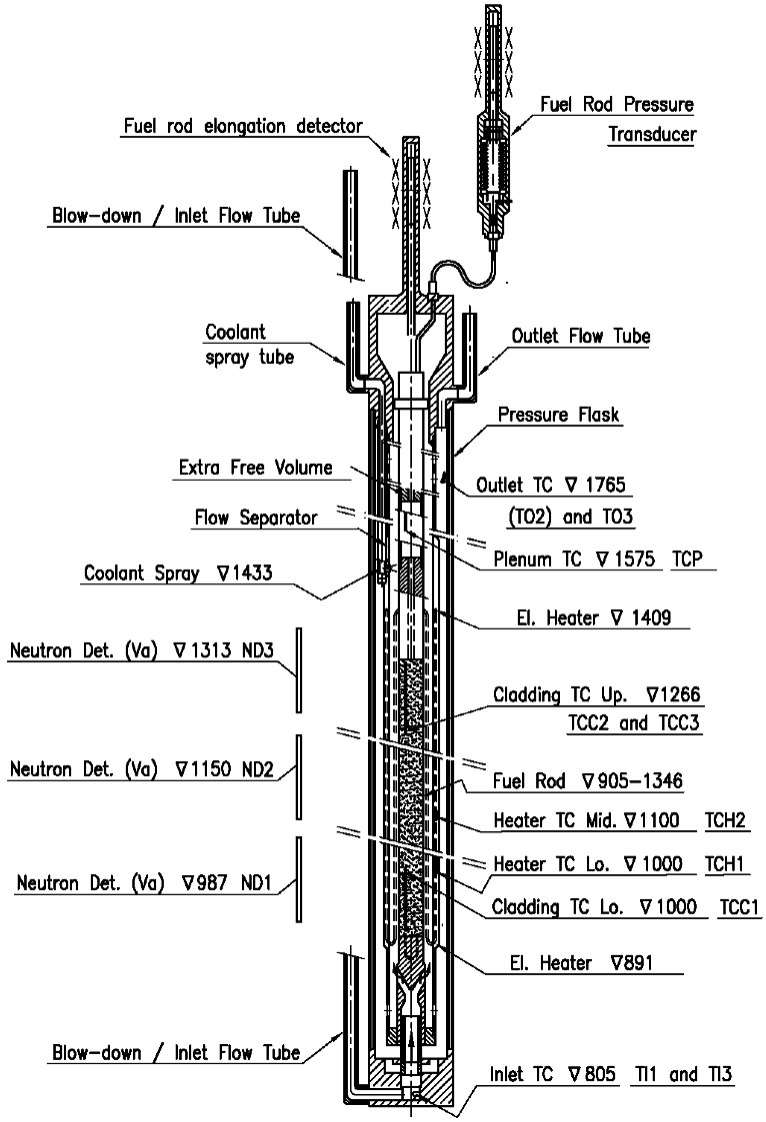

Figure 2.28: Schematic of the IFA-650.10 test rig with instrument elevations. Figure from [49]

.

fuel rod. In the BISON simulation, we also considered the commercial base irradiation preceding the test, as described in Sections 2.5.2 and 2.5.3.

The general test scheme of IFA-650.10 consisted of the following phases:

- Preparatory phases. The test started with a preparatory irradiation with effective water cooling. This consisted of a forced circulation phase followed by a natural circulation phase. At the start of the test, the axial power distribution was symmetric with a peak to average power factor of ~1.05 (Fig. 2.30). The forced circulation phase started with

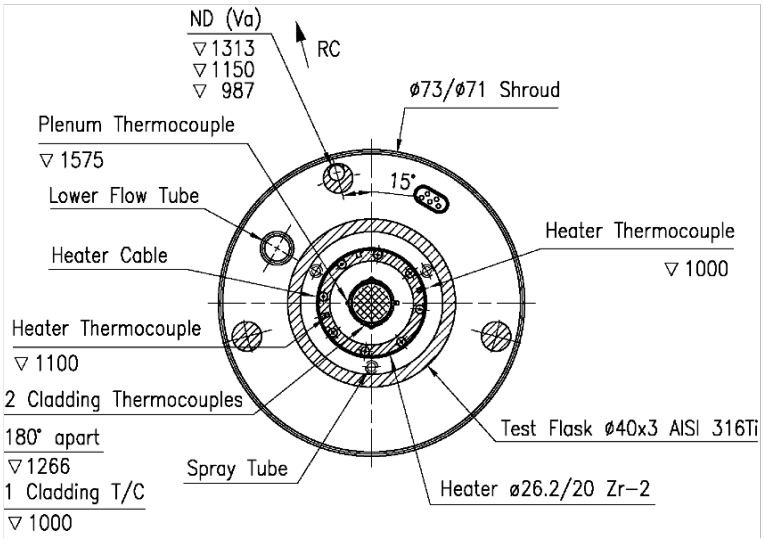

Figure 2.29: Cross sectional geometry of the IFA-650.10 test rig. Figure from [49]

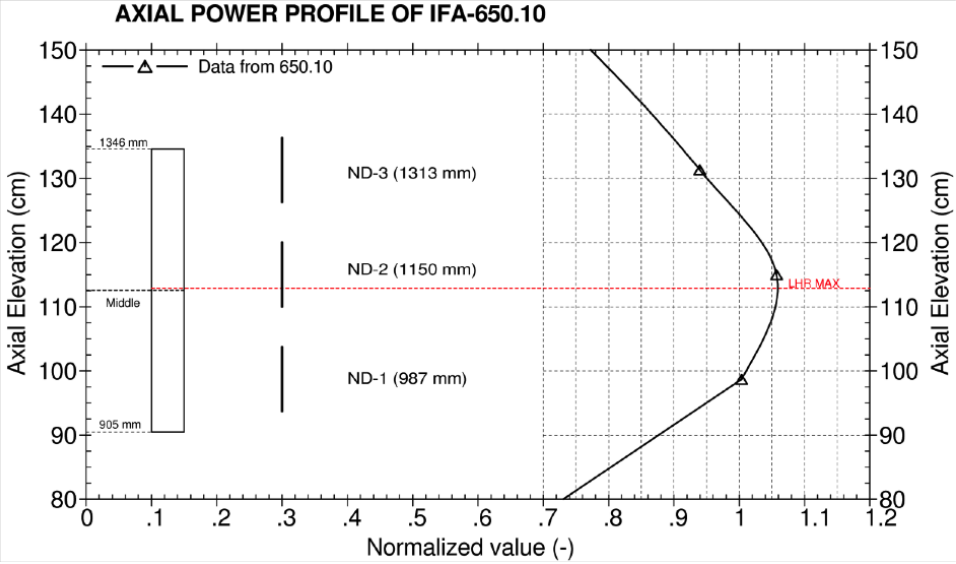

Figure 2.30: Axial power profile at the start of the test of IFA-650.10. Figure from [49]

steady state operation at a linear heat generation rate (LHGR) of 120-130 W/cm, with the outer loop connected and the pressure in the loop set to ~70 bar. Then the LHGR was decreased to ~25 W/cm by decreasing the reactor power. After reaching the correct fuel power level the electrical heater was turned on to the preset value ~12 W/cm. The power levels were chosen based on the previous test runs and pre-calculations to achieve the target peak cladding temperature (PCT) of 850 C during the heat-up phase of the test.

Then the flow regime was switched to natural circulation by disconnecting the rig from the outer loop. The flow separator enabled natural convection flow in the test section of the rig: water flowed up between the fuel rod and flow separator (with heater) and down between flow separator and flask wall. Full pressure still existed in the rig. Temperatures in the rig were left to stabilize for three minutes before blowdown.

- Blowdown phase. Valves to the dump tank were opened (blowdown). The channel pressure decreased rapidly to ~4 bar as water flew out of the pressure flask. The rig was practically emptied of water in ~71 s, which corresponds to the end of the blowdown phase (beginning of the dry phase). The end of the blowdown phase is identified by the sudden increase in cladding and heater surface temperature. Also the temperature difference between the cladding and heater increases rapidly at end of the blowdown phase.
- Dry or heat-up phase. Stagnant superheated steam surrounding the test rod provided inadequate cooling and the fuel cladding temperature increased quickly. Much of the heat removal from the test rod is by radiation to the surrounding heater. Small amounts of water are periodically sprayed into the rig to maintain a sufficient amount of steam for cladding oxidation during this phase. The influence of spraying on measured cladding, heater and coolant temperatures is reported to be weak, but no quantitative information on this issue is provided. Ballooning and burst occurred during the heat-up phase and were detected from pressure and temperature signals (burst at ~1025 K, ~249 s after blowdown). The test was ended by a reactor scram 418 s after the blowdown.

2.5.1.3 Test results

The test was carried out successfully in May 2010. The test facility with its instruments worked well and cladding ballooning and burst occurred.

After the blowdown was completed (beginning of the dry or heat-up phase), an increase in the internal pressure and cladding temperatures was observed. At the beginning of the heat-up phase, and starting from a temperature of ~460 K, the average cladding temperature increase rate was ~5 K/s for TCC1 and ~4.3 K/s for TCC2 and TCC3. This rate slowly decreased until the burst, when it was approximately 1 K/s for all the thermocouples. The evolution of cladding, heater and coolant temperature signals during the phases of the experiment are reported in Fig. 2.31.

Rod inner pressure in hot conditions was ~70 bar. Cladding ballooning started 228 seconds after the blowdown initiation (Fig. 2.32). The burst occurred 249 sec after the beginning of the blowdown. The burst time is recognizable as corresponding to the drop of the internal pressure signal and also, by the increase in activity indicated by the gamma monitor ~5 sec after the burst.

During post-irradiation examinations (PIE), the cladding outer diameter profile for IFA-650.10 was measured, which can be compared to code calculations for the mechanical behavior (ballooning) of the cladding. Figure 2.33 shown a visual inspection of the IFA-650 fuel rod around the burst opening.

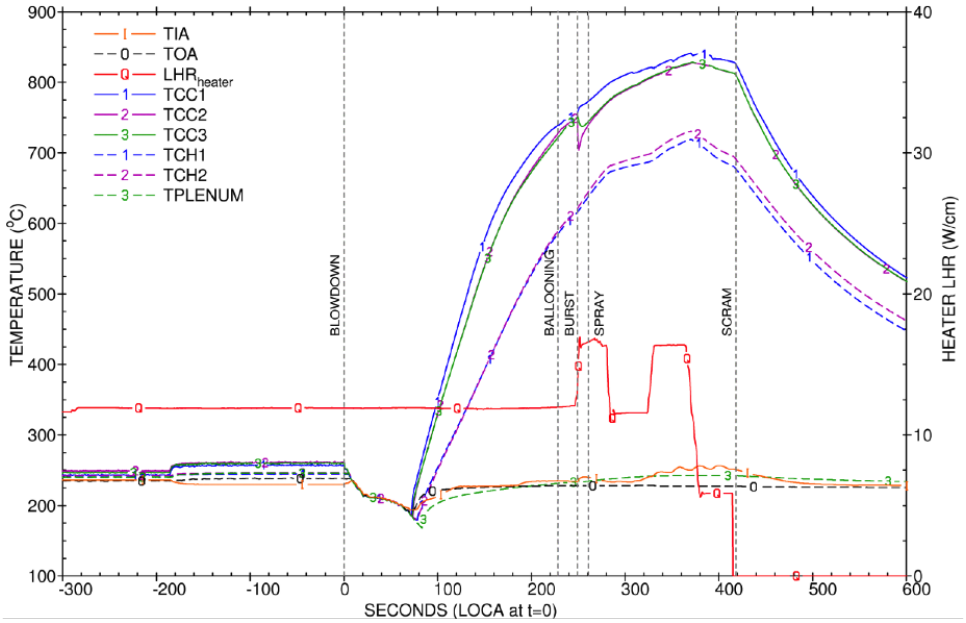

Figure 2.31: Signals for measured cladding (TCC), heater (TCH), coolant inlet (TIA) and outlet (TOA) temperatures, and heater power (LHR_{heater}) during the IFA-650.10 test. Taken from [49].

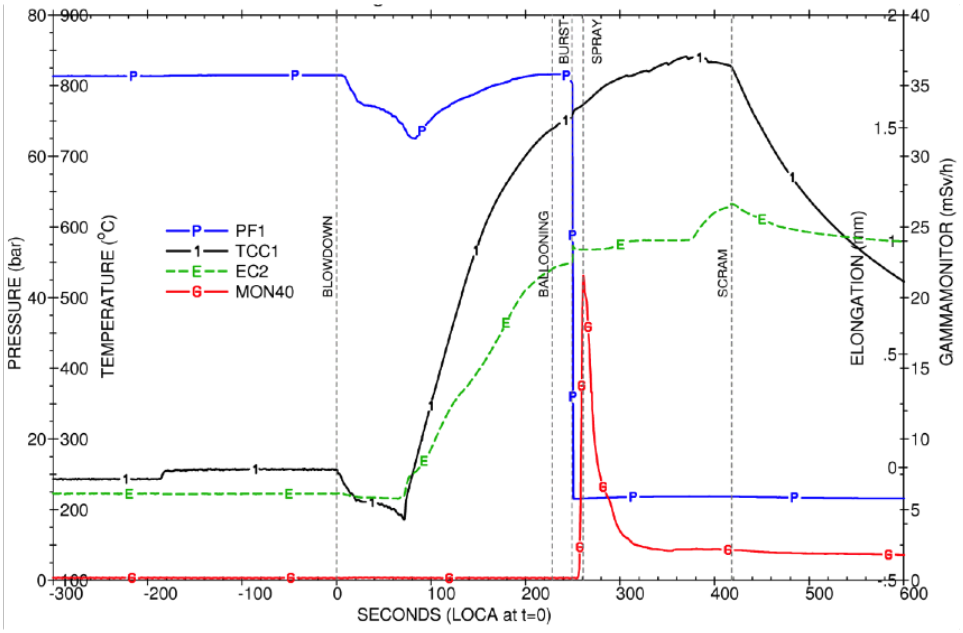

Figure 2.32: Signals for measured rod inner pressure (PF1), clad temperature (TCC), elongation (EC2) and gamma monitor response in the blow-down line (MON40). Taken from [49].

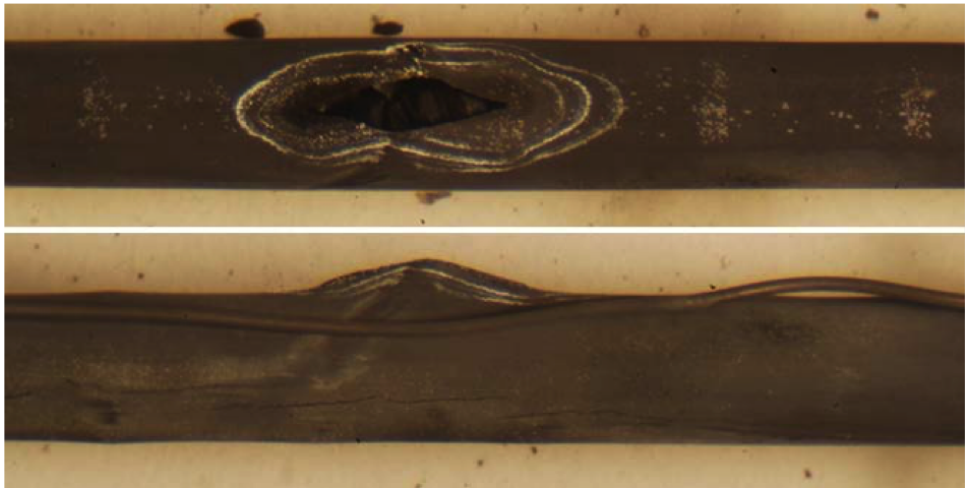

Figure 2.33: Post-test visual inspection for IFA-650.10 showing burst opening at two orthogonal orientations.

2.5.2 The BISON computational model for IFA-650.10

A 2D BISON model of the IFA-650.2 fuel rod was constructed. The geometric parameters specified in Table 2.6 were used to develop a BISON finite-element mesh that suitably represents the experimental rod, including the fuel column, cladding tube, and plenum volumes. The fuel was meshed as a smeared column with 12 radial elements and 88 axial elements. The cladding was meshed with 4 radial elements and 176 axial elements. Linear (Quad4) elements were used. The plenum length was adjusted such that the initial rod inner volume is equal to the value of 17 cubic centimeters given in the documentation for the experiment [49,50]. The BISON computational mesh for the simulation of IFA-650.10 is shown in Fig. 2.34. For simplicity, the base irradiation was simulated on the geometry of the refabricated IFA-650.10 rod rather than on the geometry of the original commercial mother rod.

The plastic instability criterion for cladding burst failure (Section 1.4) was chosen for this simulation, as it was found to be the most appropriate for the analysis of pre-irradiated fuel rod experiments.

Refabrication in BISON is accounted for by specifying the refabrication temperature, pressure, and volume to suitably reset the rod conditions at the time of refabrication.

As for the time-dependent boundary conditions such as linear power, coolant pressure histories, and thermal boundary conditions at the cladding outer wall, clearly their accurate determination is crucial to the reliability of the experiment simulation. The work performed at INL on evaluating the time-dependent boundary conditions to inform the BISON simulation of IFA-650.10 is described in the next section.

2.5.3 Time-dependent boundary conditions

Commercial base irradiation

Simulation of the commercial base irradiation was included in the BISON analysis of IFA-650.10. The power history for the base irradiation was made available to FUMAC by the Halden Project in chart form and is reported in Fig. 2.35. The power data were digitized from this chart and tabulated for usage as input to BISON. As for the coolant conditions during the base irradiation, typical PWR parameters were adopted, i.e.: water at a pressure of 15.5 MPa, an inlet temperature of 580 K and an inlet mass flux of 3800 kg/m^2-s was considered. The heat transfer from the cladding to the coolant was modeled using BISON's internal coolant channel model for convective heat transfer under PWR conditions.

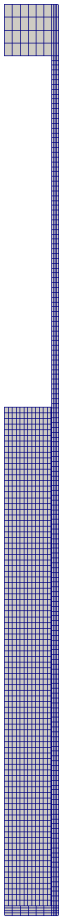

Figure 2.34: BISON computational finite-element mesh for the IFA-650.10 fuel rod. The view is magnified 10 times in the radial direction for improved visualization.

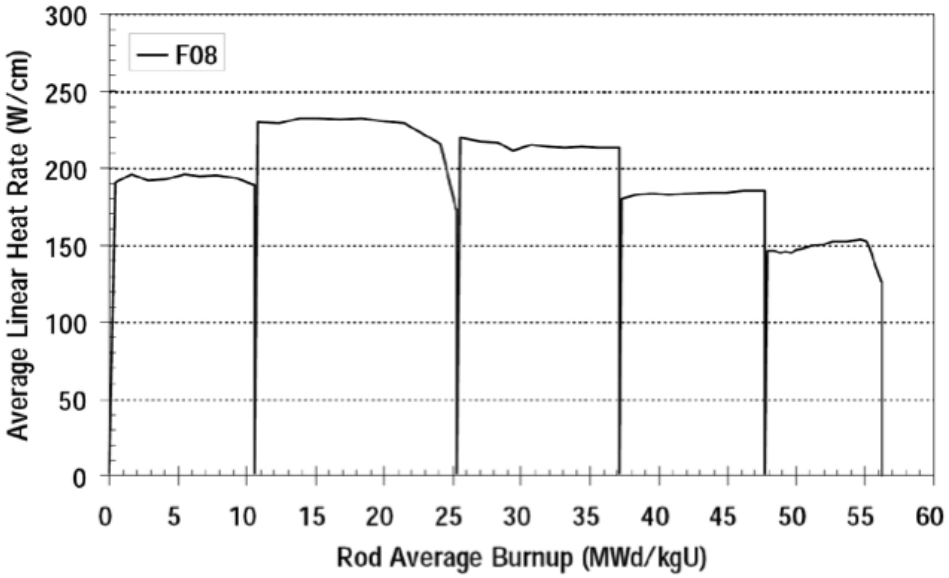

Figure 2.35: Power history for the commercial base irradiation of IFA-650.10

Halden test – Preparatory phases

As outlined in Section 2.5.1.2, the Halden test began with preparatory phases of fuel rod irradiation under coolant conditions of forced circulation, first, and natural circulation, afterwards. Since the SOCRAT calculations do not cover these preparatory phases [48], an alternative approach was adopted at INL to determine the temperature boundary conditions at the cladding outer surface. In particular, rather than explicitly modeling the cladding-to-coolant heat transfer during these preparatory phases, we chose a pragmatic approach in which we used the measured temperatures available from the Halden data. In particular, for these initial phases of the experiment, we considered an axially flat temperature profile, with the (time dependent) temperature value being the average of the temperature data measured at two different axial locations (Section 2.5.1). The temperature profile along the plenum length is also considered as flat, with the temperature value being equal to the temperature measured by the third thermocouple, which was placed at the axial midplane of the plenum (Section 2.5).

This approach guarantees good accuracy as the temperature values are derived directly from the measurements. The downside of this approach is that axial temperature peaking (which is associated with power peaking) is not allowed as an axially flat profile is used. This makes such an approach less suitable for the post-blowdown phases of the test (i.e., the blowdown phase and the heat-up phase), when cladding ballooning occurs that presents an axial dependence (localized ballooning and burst in correspondence of the hottest axial position). This is a consequence of the axial temperature peaking in the cladding and the strong temperature dependence of Zircaloy thermal creep and the associated cladding ballooning. Hence, more detailed BCs are needed for the post-blowdown phases (see Section 2.5.3). However, axial peaking is not anticipated to be

important during the low-temperature, preparatory phases of the test, when no ballooning of the cladding is involved. Basically, the simulation of the preparatory phases only serves the purpose of determining the initial temperature and rod inner pressure conditions for the subsequent post-blowdown phases. Therefore, the approach based on measured temperatures is thought to be ideal as it allows one to minimize uncertainty in the temperature boundary condition for the simulation utilizing an axially flat profile, sufficient for the purpose of analyzing the preparatory phases of the test.

As for the rod LHGR and coolant pressure histories, these were also obtained from Halden as measured time-dependent data and tabulated for usage to inform the BISON simulation.

Halden test – Blowdown and heat-up phases

The SOCRAT calculated cladding outer temperatures were used from a time 50 s before the beginning of blowdown onwards (i.e., for the time period when SOCRAT calculated temperatures are available) [48].

Figure 2.36 shows the comparison of the cladding outer temperatures compared to the Halden measurements at the axial locations where the measurements were performed. These compar-

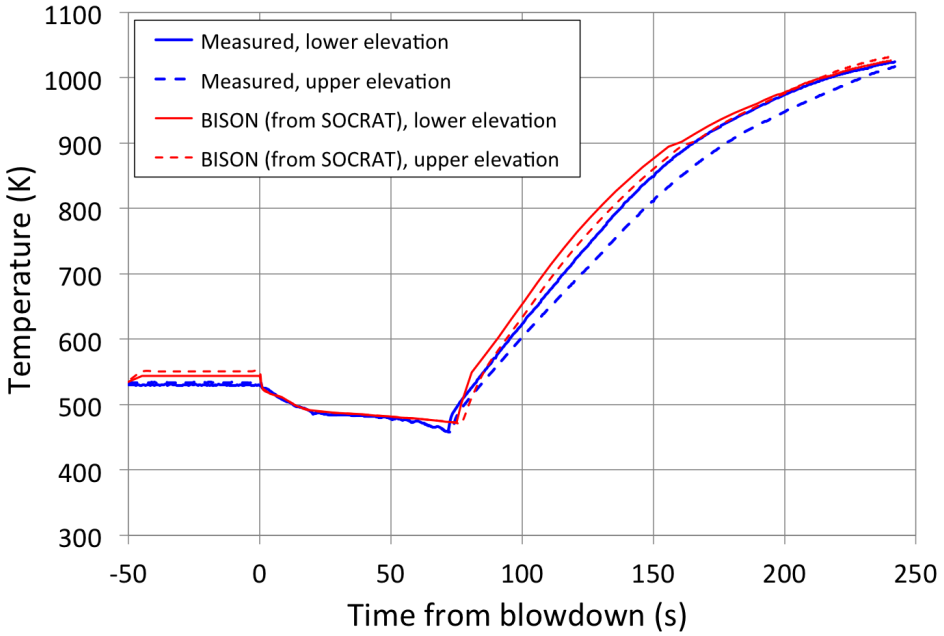

Figure 2.36: Measured cladding outer temperatures at two different axial locations in the IFA-650.10 rod during the post-blowdown phases of the test and corresponding temperatures in BISON (from the SOCRAT calculations [48])

isons correspond to those in [48] and confirm that the SOCRAT data were supplied correctly to BISON.

As for the linear heat generation rate (LHGR) history for the rod, this was obtained from Halden as raw data from neutron detector measurements. In particular, Halden provided experimental measurements as a fast-scan recording (two per second). The time-dependent LHGR raw data were tabulated for usage in BISON. The data were provided at 5 axial locations. The full information, i.e., data at all locations, was used for the BISON simulation in order to allow for the axial power peaking profile. Linear interpolation of the data along the axial direction was performed in order to obtain the rod power profile at each time step. The most recent power data provided by Wolfgang Wiesenack and that were changed in accordance with the SOCRAT calculations [47] were used.

Note that the experimental transient continued beyond the time of burst (Fig. 2.31), but we stop the simulation at burst time. After burst, factors such as the geometry of the burst opening, fuel rod depressurization, and possible fuel dispersal all affect fuel rod behavior. In this work, we rather focus on predicting pre-burst fuel rod behavior (temperatures, ballooning) as well as the time to burst.

2.5.4 Results

The BISON simulation covers all of the the phases of the IFA-650.10 experiment (Section 2.5.1.2), from the base irradiation to the LOCA transient up to the burst failure of the fuel rod cladding.

2.5.4.1 Temperature distributions in the fuel rod

Figure 2.37 shows contour plots of calculated fuel temperatures in the fuel rod at the time during the simulations that corresponds to the predicted cladding burst failure. Besides the full rod, separate plots for the fuel and cladding are shown with specific color scales. The cladding reaches very high temperatures compared to normal PWR operation values of around 600 K because of the degraded heat transfer to the coolant during a LOCA that ultimately causes cladding heat-up and ballooning due to thermal creep. These effects are consistently reproduced in the BISON simulation.

2.5.4.2 Cladding ballooning and burst behavior

Figure 2.38 shows a contour plot of calculated hoop strain at the time of burst. This corresponds to the final time of the simulation and occurs in hot conditions during the LOCA transient. The figure demonstrates how cladding ballooning, with large cladding strain and a maximum localized near the axial mid-plane of the fuel stack, is reproduced by BISON.

In order to give an account of the kinetics of the ballooning process as reproduced in the simulation, Fig. 2.39 shows the calculated time evolution of the hoop strain in the cladding (specifically,

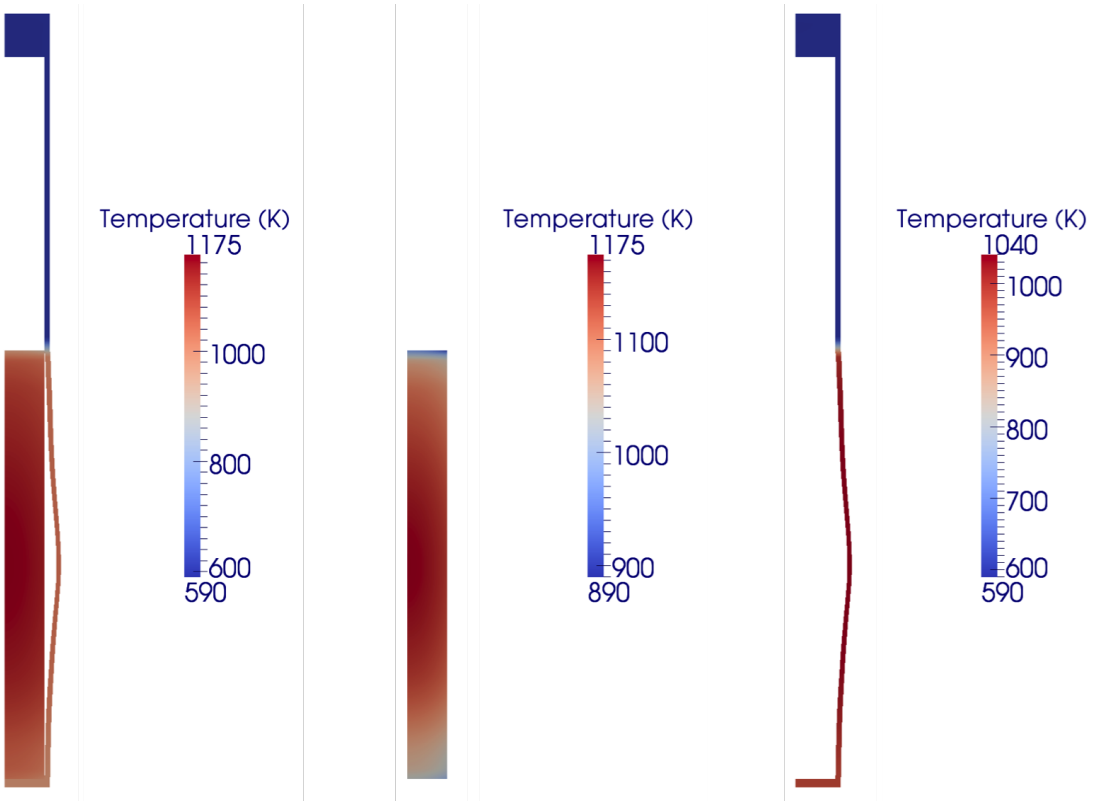

Figure 2.37: Contour plots of calculated temperature in the in the IFA-650.10 fuel rod at the time of cladding burst failure. Full rod (left), fuel only (center) and cladding only (right). The view is magnified 10 times in the radial direction for improved visualization.

at the outer surface) during the heat-up phase of the IFA-650.10 experiment. The corresponding peak outer cladding temperature is also shown. The cladding strain rapidly accelerates (ballooning) with increasing temperature during the last ~100 s before burst. This behavior ensues primarily from the exponential dependence of Zircaloy cladding creep upon temperature (Section 1.3). This kinetics is qualitatively consistent with the behavior observed experimentally during separate-effects cladding ballooning tests [44]. Rapid thermal creep and ballooning continue until the cladding fails due to burst at the location of maximum strain. BISON predicts cladding burst failure according to the plastic instability criterion as the strain rate reaches the limit level. Cladding burst is predicted to occur ~240.5 seconds after blowdown, i.e., within 9 seconds of the time observed experimentally (249 s after blowdown). Furthermore, BISON's prediction is conservative as cladding is predicted to fail before it was experimentally observed.

At the time of calculated burst failure, outer cladding temperatures in the BISON model at the axial positions of the lower and upper thermocouples were 753 and 759 C, respectively. These compare reasonably well to the measured temperatures for the lower and (average of the 3) upper thermocouples of 755 and 749 C, respectively.

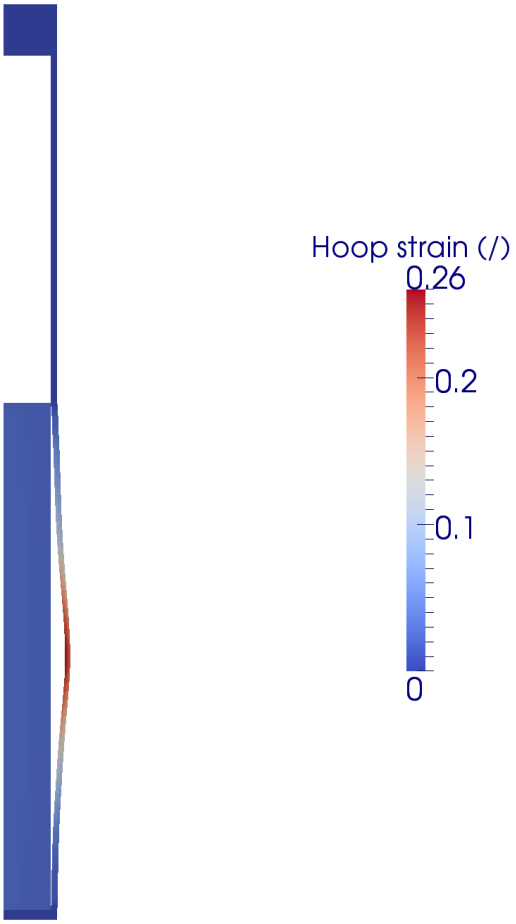

Figure 2.38: Contour plot of calculated hoop strain in the IFA-650.10 fuel rod at the time of cladding burst failure. Cladding ballooning as reproduced in the simulation is evident. The view is magnified 10 times in the radial direction for improved visualization.

Figure 2.40 shows the axial profile of the cladding diameter at the end of the simulation compared with the experimental data from post-irradiation examinations. BISON is able to predict cladding ballooning with a physically meaningful profile and with the position of maximum strain being reasonably close to the experimental observation. However, an over-prediction of cladding outward strain along the rod is observed.

As already noted in Section 2.1.3, the accurate prediction of maximum cladding strains reached during LOCA tests is extremely difficult. In particular, very high strain rates are attained as cladding burst is approached (e.g., Figure 2.39, Figure 2.11), which implies that the maximum strain reached in the calculation is very sensitive to the specific criterion adopted to determine the time of rod burst (thus, the final time of the calculation and the time at which strain is considered), since small differences in the final time may correspond to large differences in the maximum strain (see also [21]). It follows that the predicted cladding strains are sensitive

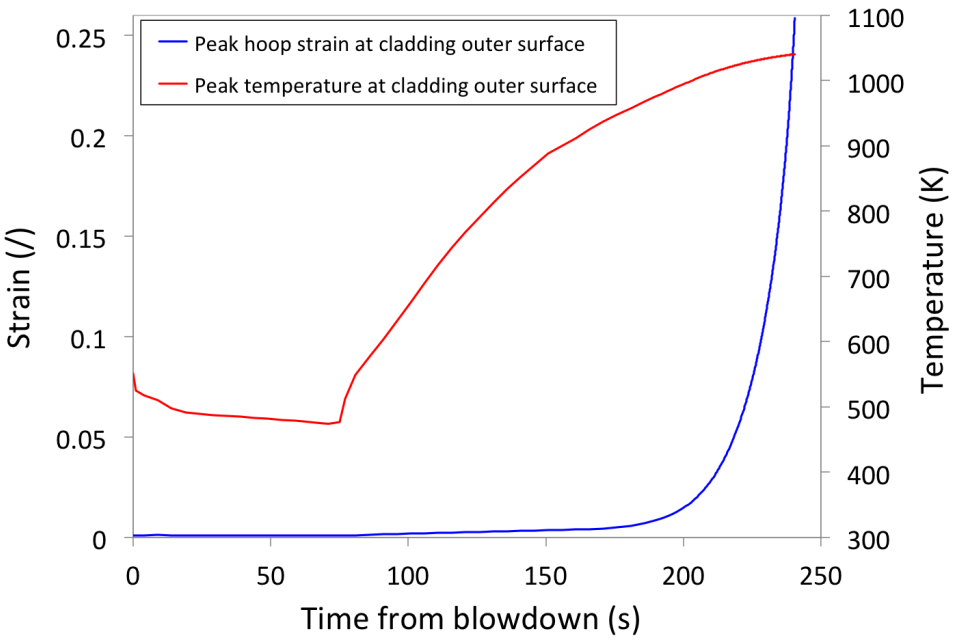

Figure 2.39: Calculated hoop strain and cladding temperature at peak axial position during the post-blowdown phases of IFA-650.10.

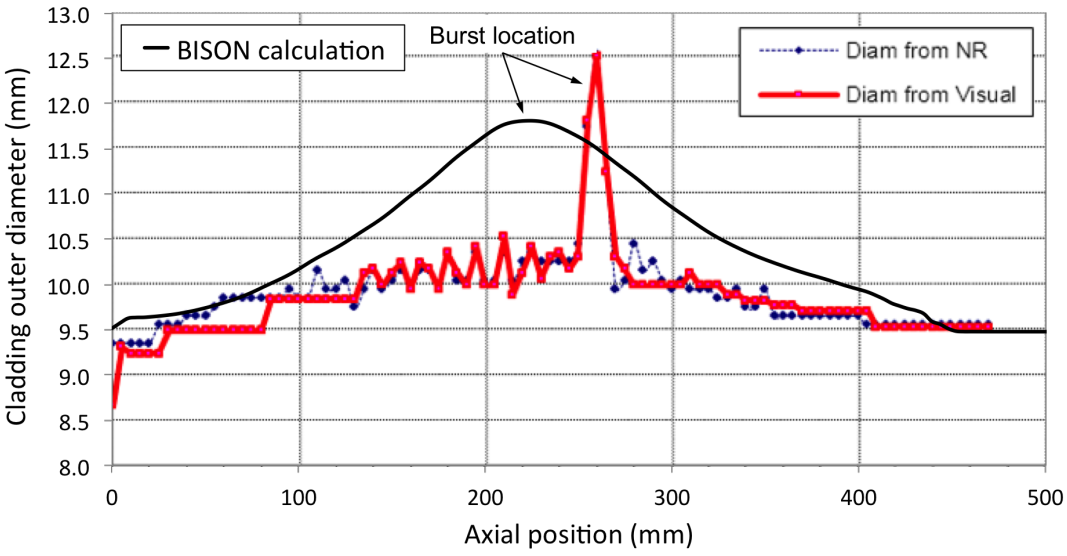

Figure 2.40: Calculated cladding outer diameter profile for IFA-650.10 at the end of the simulation compared to the PIE experimental data.

not only to the specific choice of the burst criterion but also the uncertainties in the interacting models and parameters (e.g., creep model, temperature). In order to potentially improve cladding strain predictions with BISON, further investigation and sensitivity analysis of the dependence of calculated strains upon the choice of the burst criterion, as well as further developments of the cladding creep model (e.g., considering anisotropic creep), are of interest in perspective.

2.5.4.3 Rod inner pressure evolution

In Figure 2.41, the calculated time evolution of rod inner pressure during the post-blowdown phases of the IFA-650.10 experiment is compared to the experimental (pressure transducer) data from Halden. BISON reproduces the experimental behavior with a good accuracy. A moderate over-prediction of the rod pressure during the heat-up phase is observed, which may be partly due to a discrepancy between the calculated and actual plenum temperature (which together with rod inner volume and gas content determines the plenum pressure) in consequence of the assumptions made for the estimation of the temperature boundary conditions (Section 2.5.3). Also, the calculated pressure as burst time is approached decreases more rapidly than experimentally observed. This is expected to be a consequence of calculated cladding outward deformation (ballooning) and the associated increase in rod inner volume being more pronounced than occurred experimentally. This circumstance is confirmed by the calculated cladding diameter profile at the end of the simulation shown in Fig. 2.40. An improved treatment of cladding creep that allows for anisotropic behavior, and a refined calculation of the plenum temperature, may improve our results.

As already mentioned above, the time to burst failure is predicted to be ~9 seconds before experimentally observed, which is both accurate and conservative.

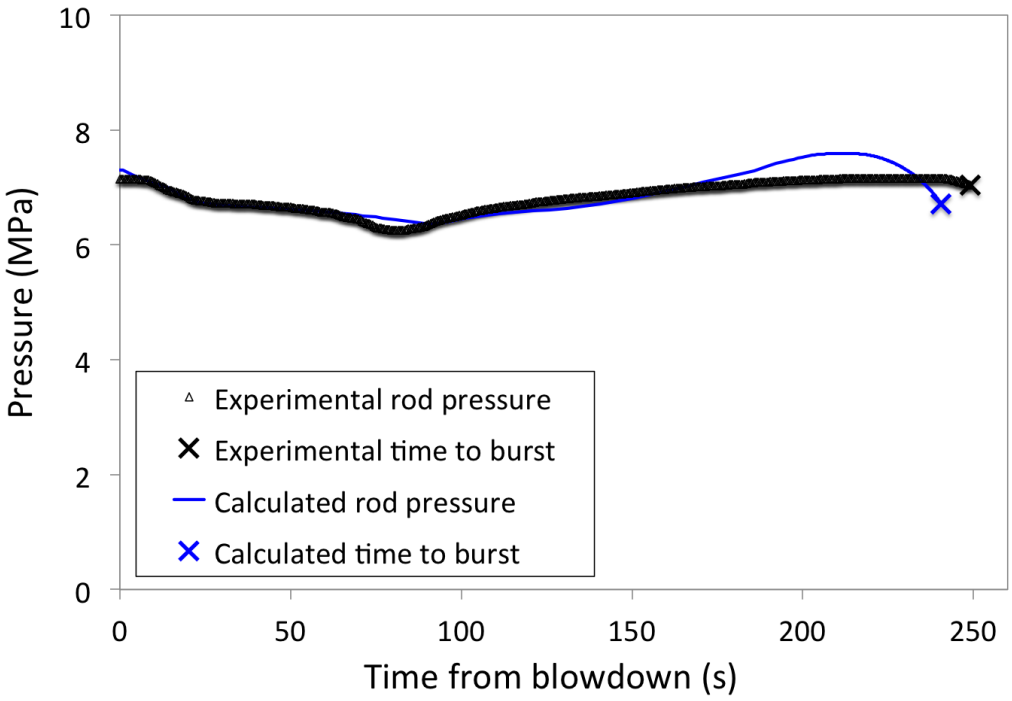

Figure 2.41: Rod inner pressure evolution during the post-blowdown phase of IFA-650.10 and time to cladding burst. BISON results are compared to the Halden experimental data.

Conclusions and Recommendations

This report summarized the contribution of Idaho National laboratory (INL) to the FUMAC project. In line with the original research agreement, work at INL has focused on both (i) developments of INL's fuel performance code BISON for the analysis of LOCAs and (ii) simulations of selected FUMAC priority cases.

As for code developments, BISON extensions relevant to FUMAC included the incorporation into the code of the key material and behavior models required to address transient high-temperature phenomena occurring during LOCAs. In particular, models were implemented in BISON for high temperature cladding oxidation, Zircaloy solid-solid phase transformation, Zircaloy high temperature creep, cladding burst failure and axial fuel relocation.

With reference to the simulation of the FUMAC cases with BISON, as originally agreed several cases were considered, including both separate effects and integral fuel rod tests. In particular, BISON simulations were performed for the FUMAC cases (1) MTA-EK tests PUZRY, (2) QUENCH L1 rods 4 and 7, (3) Halden IFA-650.2, and (4) Halden IFA-650.10. In addition, simulations of the ballooning tests REBEKA were performed and are included in this report, in view of the potential interest to the FUMAC project. This additional work included 3D simulations accounting for azimuthal temperature variations.

All of the 31 MTA-EK separate effects balloning and burst tests PUZRY were simulated with BISON. Results were reasonable in terms of cladding burst times and pressures. It was observed that discrepancies between calculations and experimental data may be partly due to anisotropic creep behavior, which is not considered in the BISON model at this time. Predictions of maximum cladding strain were less satisfactory, indicating an area of potential future improvement. It was emphasized that the accurate prediction of cladding strains reached during LOCA tests is extremely difficult, because very high strain rates are attained as cladding burst is approached, making the maximum strain reached during the calculation very sensitive to the specific burst criterion adopted and the relative uncertainties.

Additional separate effects simulations were performed for the REBEKA tests, which also pointed out a reasonable accuracy of BISON burst predictions (burst temperatures). Also, using BISON's 3D capability, one of the REBEKA cases was simulated in 3D, to investigate cladding response in presence of azimuthal temperature variations. Results indicated 3D effects are potentially important to accurate fuel rod analysis during LOCAs.

BISON simulations of the QUENCH L1 rods 4 and 7 confirmed a good predictive capability of the code for cladding burst temperatures and pressures, and less satisfactory predictions of cladding strains. In particular, maximum cladding hoop strains were underpredicted. As noted

above, this is expected to be to a significant extent related to the high sensitivity of calculated maximum strains to the choice of and uncertainties in the cladding burst criterion.

Simulation of the Halden test IFA-650.2 was also presented. This involved determination of the thermal boundary conditions at the cladding outer wall following an approximate calculation procedure based on the Halden thermocouple data. Results were compared to experimental data of rod inner pressure evolution during the test and time to cladding burst. Both quantities were reasonably well predicted by BISON. Rod pressure was slightly over-predicted during the heat-up phase of the test, which may be ascribed to discrepancies in the calculated plenum temperature and/or evolution of fuel rod inner volume during ballooning. Calculated time to burst was ~7 s before the experimental one.

Finally, we presented the BISON simulation of the Halden IFA-650.10 case. The calculation included all of the phases of the experiment from the beginning of life through the commercial base irradiation and the LOCA test. The analysis of the LOCA test was informed with the thermal boundary conditions calculated with the SOCRAT code and provided through FUMAC. The time to cladding burst failure was predicted with a good accuracy, the calculated time being within 9 seconds of the experimental one. Furthermore, the calculation was conservative, the predicted failure time being slightly earlier than experimentally observed. Also, a comparison of the cladding diameter profile at the end of the test was shown, pointing out significant discrepancies between experimental and calculated profiles. However, cladding ballooning was reproduced, with a physically meaningful profile. Finally, BISON was able to reproduce the experimental evolution of rod inner pressure during the test with a good accuracy.

BISON results are made available to the FUMAC project as a contribution to the FUMAC benchmark exercise.

In perspective, further developments of BISON for LOCA analysis are of interest in order to enhance the code's predictive capability for LOCAs. In particular, further investigation and sensitivity analysis of the dependence of calculated maximum cladding strains upon the choice of the burst criterion is deemed useful. Also, improvements in predictions of cladding strain as well as cladding burst may be achieved by considering the anisotropic creep behavior of alpha-Zr under LOCA conditions. This will require modifying the mechanics treatment in the code to consider anisotropic creep strain. Another potential source of discrepancy is the 2D representation of fuel rod behavior that involves inherently 3D effects such as localized ballooning and burst associated with azimuthal temperature variations. As demonstrated by initial 3D simulations with BISON, 3D effects are important for LOCA analysis. Additional simulations in 3D wih BISON to further investigate such effects are of interest in perspective.

Currently, BISON does not consider the thinning of the cladding metal wall during oxidation, which can be of importance to cladding mechanical behavior for the high oxidation rates that can be attained during LOCAs. This could be considered in a finite element code using the Extended Finite Element Method (X-FEM) to simulate a moving material interface (metal, oxide). Preliminary work has been performed at INL on implementing a moving material interface in BISON with X-FEM.

Also, internal cladding oxidation is not considered at this time and is of interest for future developments. Moreover, a model for hydrogen production and uptake during oxidation is available in BISON and has been applied to fuel rod lifecycle simulations including spent fuel storage [51]. However, this model has not been applied yet to LOCA simulations with BISON, and represents a potential future application.

Finally, coupling to thermal-hydraulics system codes (such as the RELAP-7 code under development at INL) is of potential interest for an improved multiphysics coupling that could result in improved boundary conditions for the BISON fuel rod calculations under accident conditions.

Acknowledgments

This work was funded by the US DOE Nuclear Energy Advanced Modeling and Simulation (NEAMS) program, the US DOE Consortium for Advanced Simulation of Light Water Reactors (CASL) project, and the INL Laboratory Directed Research and Development (LDRD) program. The submitted manuscript has been authored by a contractor of the U.S. Government under Contract DE-AC07-05ID14517. Accordingly, the U.S. Government retains a non-exclusive, royalty free license to publish or reproduce the published form of this contribution, or allow others to do so, for U.S. Government purposes.

References

[1] R. L. Williamson, J. D. Hales, S. R. Novascone, M. R. Tonks, D. R. Gaston, C. J. Permann, D. Andrs, and R. C. Martineau. Multidimensional multiphysics simulation of nuclear fuel behavior. *Journal of Nuclear Materials*, 423:149–163, 2012.

[2] R. L. Williamson, K. A. Gamble, D. M. Perez, S. R. Novascone, G. Pastore, R. J. Gardner, J. D. Hales, W. Liu, and A. Mai. Validating the BISON fuel performance code to integral LWR experiments. *Nuclear Engineering and Design*, 301:232–244, 2016.

[3] G. Pastore, S. R. Novascone, R. L. Williamson, J. D. Hales, B. W. Spencer, and D. S. Stafford. Modelling of fuel behaviour during loss-of-coolant accidents using the BISON code. In *Proc. of the LWR Fuel Performance Meeting, Zurich, Switzerland, September 13–17*, 2015.

[4] G. Pastore, R. L. Williamson, S. R. Novascone, B. W. Spencer, and J. D. Hales. Modelling of LOCA tests with the BISON fuel performance code. In *Enlarged Halden Programme Group Meeting, Fornebu, Norway, May 8–13*, 2016.

[5] R. L. Williamson, C. P. Folsom, G. Pastore, and S. Veearaghavan. Reactivity insertion accident (RIA) capability status in the BISON fuel performance code. Technical Report CASL-X-2016-1104-000, July 2016.

[6] G. Pastore, C. P. Folsom, R. L. Williamson, J. D. Hales, L. Luzzi, D. Pizzocri, and T. Barani. Modelling fission gas behaviour with the BISON fuel performance code. In *Enlarged Halden Programme Group Meeting, Lillehammer, Norway, September 24–29*, 2017.

[7] US DOE Participation in the FUMAC Coordinated Research Project on Fuel Performance Modeling, 2014. Proposal for research agreement between Battelle Energy Alliance and International Atomic Energy Agency for the FUMAC Coordinated Research Project.

[8] G. Pastore, D. Pizzocri, S. R. Novascone, D. M. Perez, B. W. Spencer, R.L. Williamson, P. Van Uffelen, and L. Luzzi. Modelling of transient fission gas behaviour in oxide fuel and application to the BISON code. In *Enlarged Halden Programme Group Meeting, Røros, Norway, September 7–12*, 2014.

[9] T. Barani, E. Bruschi, D. Pizzocri, G. Pastore, P. Van Uffelen, R.L. Williamson, and L. Luzzi. Analysis of transient fission gas behaviour in oxide fuel using BISON and TRANSURANUS. *Journal of Nuclear Materials*, 486:96–110, 2017.

[10] G. Schanz. Recommendations and supporting information on the choice of zirconium oxidation models in severe accident codes. Technical Report FZKA 6827, SAM-COLOSS-P043, Forschungszentrum Karlsruhe, Germany, 2003.

[11] S. Leistikow, G. Schanz, H. v. Berg, and A.E. Aly. Comprehensive presentation of extended Zircaloy-4/steam oxidation results 600-1600 C. In *CSNI/IAEA specialists meeting on water reactor fuel safety and fission product release in off-normal and accident conditions*, Risø National Laboratory, Denmark, 1983.

[12] J. V. Cathcart, R. E. Pawel, R. A. McKee, R. E. Druschel, G. J. Yurek, J. J. Campbell, and S. H. Jury. Zirconium metal-water oxidation kinetics, IV. Reaction rate studies. Technical Report ORNL/NUREG-17, Oak Ridge National Laboratory, 1977.

[13] J. T. Prater and E. L. Courtright. Zircaloy-4 oxidation at 1300 to 2400 C. Technical Report NUREG/CR-4889, PNL-6166, Pacific Northwest National Laboratory, 1987.

[14] A.R. Massih. Transformation kinetics of zirconium alloys under non-isothermal conditions. *Journal of Nuclear Materials*, 384:330–335, 2009.

[15] A.R. Massih and L.O. Jernkvist. Transformation kinetics of alloys under non-isothermal conditions. *Modelling and Simulation in Materials Science and Engineering*, 17:055002 (15pp), 2009.

[16] A.R. Massih. Evaluation of loss-of-coolant accident simulation tests with the fuel rod analysis code FRAPTRAN-1.4. Technical Report TR11-008V1, Quantum Technologies AB, 2011.

[17] P. Van Uffelen, C. Győri, A. Schubert, J. van de Laar, Z. Hoózer, and G. Spykman. Extending the application range of a fuel performance code from normal operating to design basis accident conditions. *Journal of Nuclear Materials*, 383:137–143, 2008.

[18] H. J. Neitzel and H. Rosinger. The development of a burst criterion for zircaloy fuel cladding under loca conditions. Technical Report KfK 4343, Kernforschungszentrum Karlsruhe, Germany, 1980.

[19] F. J. Erbacher, H. J. Neitzel, H. Rosinger, H. Schmidt, and K. Wiehr. Burst criterion of Zircaloy fuel claddings in a loss-of-coolant accident. In *Zirconium in the Nuclear Industry, Fifth Conference, ASTM STP 754, D.G. Franklin Ed.*, pages 271–283. American Society for Testing and Materials, 1982.

[20] M. E. Markiewicz and F.J. Erbacher. Experiments on ballooning in pressurized and transiently heated Zircaloy-4 tubes. Technical Report KfK 4343, Kernforschungszentrum Karlsruhe, Germany, 1988.

[21] V. Di Marcello, A. Schubert, J. van de Laar, and P. Van Uffelen. The TRANSURANUS mechanical model for large strain analysis. *Nuclear Engineering and Design*, 276:19–29, 2014.

[22] G. Pastore, L. Luzzi, V. Di Marcello, and P. Van Uffelen. Physics-based modelling of fission gas swelling and release in UO_2 applied to integral fuel rod analysis. *Nuclear Engineering and Design*, 256:75–86, 2013.

[23] G. Pastore, L.P. Swiler, J.D. Hales, S.R. Novascone, D.M. Perez, B.W. Spencer, L. Luzzi, P. Van Uffelen, and R.L. Williamson. Uncertainty and sensitivity analysis of fission gas behavior in engineering-scale fuel modeling. *Journal of Nuclear Materials*, 465:398–408, 2015.

[24] R. M. Carroll, J. G. Morgan, R. B. Perez, and O. Sisman. Fission density, burnup, and temperature effects on fission-gas release from UO_2. *Nuclear Science and Engineering*, 38:143–155, 1969.

[25] I. J. Hastings, A. D. Smith, P. J. Fehrenbach, and T. J. Carter. Fission gas release from power-ramped UO_2 fuel. *Journal of Nuclear Materials*, 139:531–543, 1986.

[26] C. T. Walker, P. Knappik, and M. Mogensen. Fission gas release from power-ramped UO_2 fuel. *Journal of Nuclear Materials*, 161:10–23, 1988.

[27] K. Une and S. Kashibe. Fission gas release during post irradiation annealing of BWR fuels. *Journal of Nuclear Science and Technology*, 27:1002–1016, 1990.

[28] SCDAP/RELAP5-3D Code Manual. Volume 4: MATPRO a library of materials properties for light-water-reactor accident analysis. Technical Report INEEL/EXT-02-00589, Idaho National Engineering and Environmental Laboratory, 2003.

[29] L. O. Jernkvist and A. Massih. Model for axial relocation of fragmented and pulverized fuel pellets in distending fuel rods and its effects on fuel rod heat load. Technical Report SSM-2015:37, Stråls säkerhets myndigheten, 2015.

[30] O. Coindreau, F. Fichot, and J. Fleurot. Nuclear fuel rod fragmentation under accidental conditions. *Nuclear Engineering and Design*, 255:68–76, 2013.

[31] J. A. Turnbull, S. K. Yagnik, M. Hirai, D. M. Staicu, and C. T. Walker. An assessment of the fuel pulverization threshold during loca-type temperature transients. *Nuclear Science and Engineering*, 179:477–485, 2015.

[32] A. E. R. Westman. The packing of particles: Empirical equations for intermediate diameter ratios. *Journal of the American Ceramic Society*, 76(11):127–129, 2015.

[33] S. A. Pitts, S. R. Novascone, H. Chen, B. W. Spencer, S. Satpathy, R. J. Gardner, and J. D. Hales. Verify and validate 1.5d capability. Technical Report CASL-U-2017-1380-000, Consortium for Advanced Simulation of LWRs, 2017.

[34] L. O. Jernkvist and A. R. Massih. Modeling axial relocation of fragmented fuel pellets inside ballooned cladding tubes and its effects on lwr fuel rod failure behavior during loca. In *Transactions of SMIRT-23*, Manchester, UK, 2015.

[35] Y. C. Chiew and E. D. Glandt. The effect of structure on the conductivity of a dispersion. *Journal of Colloid and Interface Science*, 91(1):90–104, 1983.

[36] G. Pastore, R. L. Williamson, and J. D. Hales. Status Report on INL Contribution to FUMAC with the BISON Code. Presentation given at the Seconds Research Coordination Meeting of the FUMAC Project, Vienna, Austria, May 30 – June 2, 2016. Available at https://nucleus.iaea.org/sites/nefw-projects/fumaccrp/SitePages/Home.aspx.

[37] R. L. Williamson, G. Pastore, and J. D. Hales. Status Report on US DOE/INL Participation in the Coordinated Research Project FUMAC. Technical report, May 2016. Submitted in support of the Second Research Coordination Meeting of the FUMAC Project.

[38] D.G. Hardy. High Temperature Expansion and Rupture Behaviour of Zircaloy Tubing. In *CSNI Proceeding of the Specialist Meeting on Safety of Water Reactor Fuel Elements*, Saclay, France, October 22-24 1973.

[39] C. L. Wilson et al. LOCA simulation in NRU program: Data report for the fourth materials experiment (MT-4). Technical Report NUREG/CR-3272 (PNL-4669), Pacific Northwest Laboratory, July 1983.

[40] C. L. Wilson et al. Large-break LOCA in-reactor fuel bundle materials test MT-6A. Technical Report PNL-8829, Pacific Northwest Laboratory, September 1993.

[41] R. L. Williamson, G. Pastore, K. A. Gamble, R. J. Gardner, J. Tompkins, and W. Liu. Development of a LOCA Experimental Benchmark for BISON. Technical Report CASL-U-2017-1422-000, Consortium for Advanced Simulation of LWRs, 2017.

[42] E. Perez-Feró, Z. Hózer, T. Novotny, G. Kracz, M. Horváth, I. Nagy, A. Vimi, A. Pintér-Csordás, Cs. Győri, L. Matus, L. Vasáros, P. Windberg, and L. Maróti. Experimental Database of E110 Claddings under Accident Conditions. Technical Report EK-FRL-2012-255-01/02, Center for Energy Research, Hungarian Academy of Sciences, Budapest, Hungary, May 2013.

[43] K. Kulacsy. Communication within the FUMAC Project, March 2015.

[44] F.J. Erbacher, H.J. Neitzel, and K. Wiehr. Technical Report KfK 4781, Kernforschungszentrum Karlsruhe, Germany, 1990.

[45] J. Stuckert, M. Grobe, C. Rossger, M. Steinbruck, and M. Walter. Results of the LOCA reference bundle test QUENCH-L1 with Zircaloy-4 cladding. Technical Report KIT-SR 7651, Karlsruher Institut fur Technologie, Germany, 2015.

[46] M. Ek. LOCA Testing at Halden; The Second Experiment IFA-650.2. Technical Report HWR-813, OECD Halden Reactor Project, 2005.

[47] https://nucleus.iaea.org/sites/nefw-projects/fumaccrp/SitePages/Home.aspx.

[48] Short Information on the Results of IFA-650.10 and IFA-650.11 Calculations with SOCRAT code. Technical note, version 1. Technical report, 2016. Released to the FUMAC project. Available at https://nucleus.iaea.org/sites/nefw-projects/fumaccrp/SitePages/Home.aspx.

[49] A. Lavoil. LOCA Testing at Halden; The Tenth Experiment IFA-650.10. Technical Report HWR-974, OECD Halden Reactor Project, 2010.

[50] A. Lavoil. LOCA Experiments IFA-650.10. Technical Report EP-1650.10, OECD Halden Reactor Project, 2010.

[51] D.S. Stafford. Multidimensional simulations of hydrides during fuel rod lifecycle. *Journal of Nuclear Materials*, 466:362 – 372, 2015.